Quantum Correlation Imaging Through Scattering Media

by

James Hubble

Thesis submitted to the University of Ottawa in partial
fulfillment of the requirements for the degree of

Master of Science, Physics
Concentration in Quantum Science

Department of Physics
Faculty of Science
Ottawa-Carleton Institute of Physics
Supervisor: Dr. Ebrahim Karimi

© James Hubble, Ottawa, Canada, 2026

Abstract

This thesis explores the use of spatially entangled photon pairs to enhance imaging contrast through weakly scattering media. Particular attention is paid to how the spatial correlations of biphotons survive or degrade on propagation through a scattering medium, and to how coincidence detection combined with post-selection on those correlations can separate ballistic from scattered light. Because ballistic biphotons preserve their source correlations while scattered pairs do not, retaining only the coincidences consistent with those correlations enhances contrast relative to conventional single-photon imaging and simultaneously rejects uncorrelated background. We demonstrate this enhancement, quantified through the modulation transfer function, in two configurations — one in which both photons from the pair are affected by the scattering medium, and one in which only a single photon is scattered while its partner follows an undisturbed reference path, directly to a spatially-resolving detector, which partially compensates for the resulting increase in shot noise by combining events from several post-selection windows.

In the first chapter, a brief overview of the field is provided, introducing the concept of contrast, the problem of scattering, and the degrees of freedom of light. The second chapter develops the background necessary to understand the experiment: the quantization of the electromagnetic field, quantum entanglement, spontaneous parametric down-conversion and the spatial and temporal correlations of the biphoton state, and the quantum imaging configurations that exploit them. In the third chapter, the experimental implementation and results are presented, followed by the article reporting the method and its demonstration through weakly scattering media. Finally, the conclusions and outlooks are outlined in the last chapter.

Acknowledgements

First and foremost, I would like to thank my supervisor, Dr. Ebrahim Karimi, for being so supportive and encouraging throughout these years, for our countless academic discussions, and for instilling in me the ambition to "focus on the science". Since joining the SQO group in 2020, I have always felt encouraged by him and by the members of the group, who together foster an environment for growth and learning. I am grateful for everything he has taught me, in science and in life.

I would also like to thank all of the members of the group for making everyday life and work so enjoyable and engaging. I would especially like to thank Rojan Abolhassani, who worked alongside me on every part of this project and made even the longest days in the lab a pleasure, and Dr. Alessio D'Errico, for being an exceptional and endlessly patient mentor. Thank you both for taking so much time out of your days to teach me new things. I am also grateful to all of my collaborators, who have contributed so much to my knowledge.

Finally, I want to thank my parents and my sisters for their constant support, for always taking an interest in my work, and for cheering on even my smallest victories. This whole journey was made possible because of you.

Author Contributions and Statement of Originality

To the best of his knowledge, the author states that the work described in this Master's thesis constitutes original research in the field of physics. Below, we present each participant's collaborative contributions for each chapter.

Chapter 1: James Hubble wrote this chapter, which introduces the background and motivation for the thesis, under the supervision of Ebrahim Karimi.

Chapter 2: James Hubble wrote this theoretical chapter under the supervision of Ebrahim Karimi.

Chapter 3: Alessio D'Errico developed the theory. James Hubble, Rojan Abolhassani, and Alessio D'Errico prepared the experimental setup and performed the experiment. James Hubble, Rojan Abolhassani, and Alessio D'Errico analyzed the data for both the single-photon and two-photon scattering experiments, with Yishai Klein also analyzing the two-photon scattering data. Alessio D'Errico, Yingwen Zhang, and Ebrahim Karimi supervised the project. All authors contributed to the discussions and text of the manuscript.

Contents

Abstract **ii**

Acknowledgements **iii**

Author Contributions and Statement of Originality **iv**

Curriculum Vitae **vii**

List of Figures **viii**

List of Tables **ix**

1 Introduction **1**
- 1.1 Overview . . . 1
- 1.2 Maxwell's Equations . . . 3
- 1.3 Quantization and the Photon . . . 4
- 1.4 Degrees of Freedom . . . 5
  - 1.4.1 Polarization . . . 5
- 1.5 The Poincaré Sphere . . . 6
  - 1.5.1 Spatial Degree of Freedom . . . 8
  - 1.5.2 Temporal Degree of Freedom . . . 10
  - 1.5.3 Spectral Degree of Freedom . . . 11

2 Quantum Entanglement and Biphoton States **13**
- 2.1 Field Quantization and Optical Coherence . . . 14
- 2.2 Entanglement and Quantum States . . . 18
- 2.3 Spontaneous Parametric Down-Conversion . . . 19

2.4 The Biphoton State and its Correlations 23
2.5 Quantum Imaging with Biphotons 27

3 Entanglement-Enhanced Imaging in Scattering Environments **29**
3.1 Scattering Media 30
3.2 Biphoton Imaging 35
3.3 Correlation Imaging/Single Photon Scattering 43
3.4 Manuscript 48

4 Conclusion and Overview **61**

Bibliography **64**

Curriculum Vitae

1. A. D'Errico, **J. Hubble**, R. Abolhassani, N. Dehghan, Y. Klein, Y. Zhang, and E. Karimi, "Contrast enhanced imaging through weakly scattering media with spatially entangled photons," arXiv:2605.28998 (2026).

2. D. Paneru, A. Te'eni, B. Y. Peled, **J. Hubble**, Y. Zhang, A. Carmi, E. Cohen, and E. Karimi, "Experimental tests of multiplicative Bell inequalities and the fundamental role of local correlations," *Physical Review Research* **3**, L012025 (2021).

List of Figures

1.4.2 Laguerre–Gaussian LG modes for varying azimuthal index and radial index. . 7

2.1 Spontaneous Parametric Down-Conversion (SPDC) process. 16

2.2 Spontaneous Parametric Down-Conversion (SPDC) intensity profile in the far field. 20

2.3 Ghost imaging. 22

2.4 The Poincaré sphere. 24

3.1 Conceptual scheme. 28

3.2 Contrast enhancement with static scattering medium between object and camera. 32

3.3 Contrast enhancement with dynamic scattering media before and after object. 34

3.4 Correlation imaging with dynamic scattering media. 37

3.5 Retrieving image details by correlation post-selection. 38

List of Tables

1

Introduction

1.1 Overview

We do not see light so much as we see *differences* in light: a white cup is invisible against a white cloth but leaps out against a dark table. This separation between a feature and its background is what imaging science calls *contrast*, or visibility. If a feature reaches the

detector with intensity $I_{\max}$ and its background with $I_{\min}$ [1],

$$V = \frac{I_{\max} - I_{\min}}{I_{\max} + I_{\min}}. \tag{1.1}$$

The visibility value is between 0 and 1. For visibility near unity, the feature is extremely sharp, which occurs when the minimum intensity reaches zero, $I_{\min} = 0$. As the visibility falls toward zero, the image becomes unreadable and disappears into the background. Therefore, any worthy imaging configuration, before anything else, must preserve the contrast of the feature in which it is imaging.

Scattering is one of the most common effects that acts to degrade the visibility, or contrast, of an imaging system. In fog, turbid water, or biological tissue, part of the light travels nearly straight through the scattering media and is more weakly influenced — the *ballistic* photons — there are also photons that are scattered more strongly, experience more influence from the scattering media and arrive from all directions carrying very little information about the image. This stray, scattered light does not darken the image but brightens it uniformly, raising $I_{\min}$ while $I_{\max}$ stays fixed, so the contrast collapses; it is scattering, not absorption or diffraction, that limits how deep one can see into tissue [2].

Instead, this thesis uses quantum correlations of light to select ballistic photon pairs and to filter out the photon pairs that are more strongly influenced by the scattering medium [5]. Photon pairs from spontaneous parametric down-conversion are entangled in their transverse positions, a resource exploited from ghost imaging [6] to imaging through noise and stray light [7, 8]. The idea here is simple: ballistic biphotons keep stricter position

correlation relations in comparison to biphotons that experience stronger scattering. By recording spatially resolved coincidences, reject as much of the diffuse background as possible while constructing an image made up of primarily ballistic photons. The remainder of this chapter sets out to lay the groundwork for the physics covered in the thesis.

1.2 Maxwell's Equations

The classical description of light begins with Maxwell's equations, which govern the coupled behaviour of the electric field $\mathbf{E}$ and the magnetic field $\mathbf{B}$ [9]:

$$\nabla \times \mathbf{E} = -\frac{\partial \mathbf{B}}{\partial t}, \tag{1.2}$$

$$\nabla \times \mathbf{H} = \frac{\partial \mathbf{D}}{\partial t} + \mathbf{J}, \tag{1.3}$$

$$\nabla \cdot \mathbf{D} = \rho, \tag{1.4}$$

$$\nabla \cdot \mathbf{B} = 0. \tag{1.5}$$

where $\mathbf{D} = \varepsilon \mathbf{E}$ and $\mathbf{H} = \mathbf{B}/\mu$ in a linear medium, and ρ and $\mathbf{J}$ are the charge and current densities. In a source-free vacuum ($\rho = 0$, $\mathbf{J} = 0$), these equations decouple into wave equations for electric and magnetic fields,

$$\nabla^2 \mathbf{E} - \frac{1}{c^2} \frac{\partial^2 \mathbf{E}}{\partial t^2} = 0, \tag{1.6}$$

$$\nabla^2\mathbf{B} - \frac{1}{c^2}\frac{\partial^2\mathbf{B}}{\partial t^2} = 0. \tag{1.7}$$

describing waves that propagate at speed $c = 1/\sqrt{\mu_0\varepsilon_0}$ – here ∇^2 is Laplacian. Substituting plane-wave solutions into Maxwell's equations reveals that the electric and magnetic fields are both transverse to the direction of propagation $\mathbf{k}$ and orthogonal to one another. Their amplitudes are related by $B = E/c$. Consequently, the electric field $\mathbf{E}$, magnetic field $\mathbf{B}$, and wave vector $\mathbf{k}$ form a mutually orthogonal right-handed set of vectors. The direction of energy flow is given by the Poynting vector, $\mathbf{S} = \frac{1}{\mu_0}\mathbf{E}\times\mathbf{B}$. These properties demonstrate that light is a transverse electromagnetic wave consisting of coupled oscillating electric and magnetic fields propagating through space at the speed of light. This is light in the classical picture: a self-sustaining oscillation of the electromagnetic field. Maxwell's equations are the foundation from which every property of light used in this thesis descends, but they describe light as a continuous wave and cannot account for the discrete way in which it is emitted, absorbed, and detected.

1.3 Quantization and the Photon

At the turn of the twentieth century, classical physics hit a definitive wall in its attempts to describe blackbody radiation. While Wien's radiation law successfully modeled the high-frequency spectrum, it failed completely in the infrared domain [10]. Conversely, treating radiation classically as a continuum of standing waves led to a predicted energy density

that diverged to infinity at higher frequencies. This unphysical contradiction implied that any warm object should instantly radiate an infinite amount of high-frequency energy, a profound systemic failure that became known as the ultraviolet catastrophe [11].

Max Planck resolved this crisis by fundamentally altering how matter and radiation interact. By interpolating the successful regions of the competing classical models, he demonstrated that the empirical blackbody spectrum could only be reproduced if energy exchange with the electromagnetic field occurs in discrete, localized units proportional to frequency, $E = h\nu$ – here h is the Planck constant and ν is the electromagnetic field's frequency [12]. Albert Einstein subsequently extended this concept directly to the radiation field itself, proposing that light does not merely exchange energy in packets, but is physically composed of independent quanta—photons—each carrying distinct energy and momentum [13].

1.4 Degrees of Freedom

1.4.1 Polarization

For a plane wave propagating along the z-direction, the electric field is confined to oscillate in the transverse xy-plane. The polarization of the wave is determined by the relative amplitudes and phases of its transverse field components. Because the transverse plane is two-dimensional, two orthogonal basis vectors are sufficient to describe any polarization state. A convenient choice is the horizontal and vertical basis, $\mathbf{e}_H$ and $\mathbf{e}_V$, corresponding to

electric-field oscillations along the x- and y-axes. At the single-photon level, polarization forms a two-dimensional Hilbert space and thus provides a natural physical implementation of a qubit. An arbitrary polarization state may be written as

$$|\Psi\rangle = \alpha\,|H\rangle + \beta e^{i\phi}\,|V\rangle\,, \qquad |\alpha|^2+|\beta|^2= 1. \tag{1.8}$$

where the coefficients α and β determine the probability amplitudes associated with the horizontal and vertical polarization states, while ϕ specifies their relative phase. Particular choices give the named states: diagonal $|D\rangle$ and antidiagonal $|A\rangle$ (linear, at $\pm 45°$), and left- and right-circular $|L\rangle$, $|R\rangle$, in which the field vector rotates at fixed magnitude about the propagation axis. The circular states $|L\rangle$ and $|R\rangle$ carry spin angular momentum of $+\hbar$ and $-\hbar$ per photon along the propagation direction, respectively, where $\hbar$ is the reduced Planck constant.

1.5 The Poincaré Sphere

The polarization state of light resides in a two-dimensional Hilbert space, whose symmetry is described by the group SU(2). Because SU(2) is closely connected to the rotation group SO(3), polarization states admit a simple geometric representation on the surface of a unit sphere. This construction, known as the Poincaré sphere, offers a powerful visual language for understanding polarization and its evolution under optical transformations.

The polarization states are conveniently represented as points in or on a unit sphere —

the Poincaré sphere — through four real quantities known as the Stokes parameters [1]. In terms of the transverse field components, these are defined as:

$$S_0 = |E_x|^2 + |E_y|^2, \tag{1.9}$$

$$S_1 = |E_x|^2 - |E_y|^2, \tag{1.10}$$

$$S_2 = 2\,\mathrm{Re}(E_x^* E_y), \tag{1.11}$$

$$S_3 = 2\,\mathrm{Im}(E_x^* E_y). \tag{1.12}$$

where S_0 is the total intensity and the normalized triple $(S_1, S_2, S_3)/S_0$ gives the position on the sphere. The geometry is intuitive; The $\hat{S}_1$ axis corresponds to horizontal and vertical linear polarization; the $\hat{S}_2$ axis corresponds to diagonal and antidiagonal polarization; and the $\hat{S}_3$ axis corresponds to the left- and right-circular polarization. Every linear polarization lies on the equator, and the two circular states are located at the poles of the Poincaré sphere.

The Poincaré sphere is more than a bookkeeping device. The polarization transformations produced by wave plates and rotators correspond to rotations of the sphere, and a polarization state carried around a closed loop on its surface acquires a geometric phase equal to half the enclosed solid angle [38, 39]. This is the central object of Chapter 4, which examines rotation about the $\hat{S}_3$ axis — a transformation that carries a state around a circle of constant latitude. Establishing the sphere and its axes here provides the geometric vocabulary on which that chapter depends.

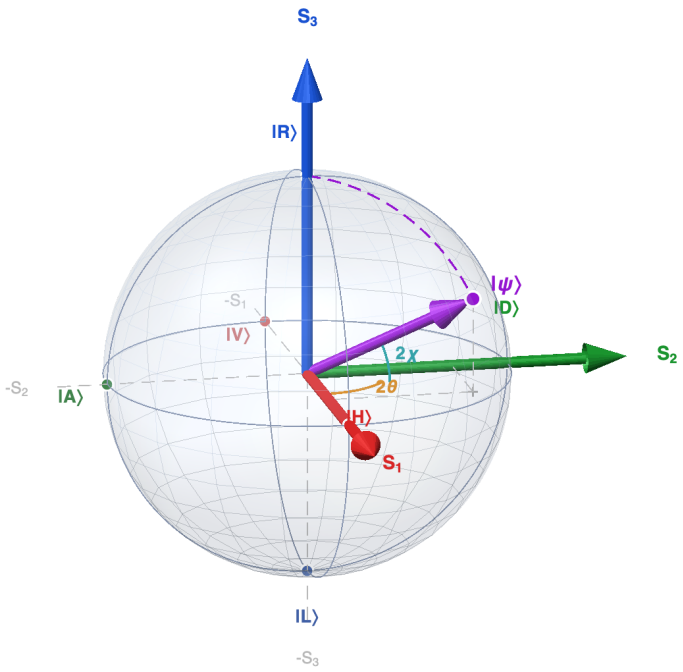


Figure 2.4. The Poincaré sphere. Every pure polarization state maps to a point on the unit sphere, whose Cartesian axes are the three Stokes parameters S_1, S_2, S_3 (normalized to the total intensity). Linear polarizations are defined to be located on the equator, and the left-circular and right-circular states are defined to be at the bottom and top poles, respectively. Elliptical polarizations are defined as polarization states that are not located solely on the equator or at the poles.

1.5.1 Spatial Degree of Freedom

Beyond polarization, light also carries information in its transverse spatial profile. When a beam propagates predominantly along the z-axis, its complex field envelope can be

described within the paraxial approximation by

$$\left(\nabla_{\perp}^{2} + 2ik\,\frac{\partial}{\partial z}\right) E(x, y, z) = 0. \tag{1.13}$$

where $\nabla_{\perp}^{2}$ denotes the transverse Laplacian. This equation follows directly from the Helmholtz equation when the field envelope varies slowly along the propagation direction, and the optical field remains confined to small angles with respect to the optical axis. Despite its apparent simplicity, the paraxial wave equation admits a rich family of solutions with distinct spatial structures. These modes provide additional degrees of freedom that can be exploited for applications ranging from classical beam shaping to high-dimensional quantum information processing. Among its solutions, the Laguerre–Gaussian modes $\mathrm{LG}_{\ell,p}$ are of particular interest because they carry a helical phase front of the form $\exp(i\ell\phi)$, where ϕ is the azimuthal coordinate and ℓ is an integer. A photon in such a mode carries orbital angular momentum (OAM) of

$$L_z = \ell\hbar. \tag{1.14}$$

along the propagation direction; the index p labels the radial structure of the mode and is not a focus of this work. Unlike polarization, which spans only two dimensions, OAM is in principle unbounded: ℓ may take any integer value, so a single photon can access an arbitrarily high-dimensional state space. This is only an introduction to the spatial degree of freedom: the full two-photon spatial wavefunction — the joint transverse state of the entangled signal and idler photons produced by spontaneous parametric down-conversion — is developed in detail in Chapter 2, and spatial correlations between photon pairs are

exploited in Chapter 3.

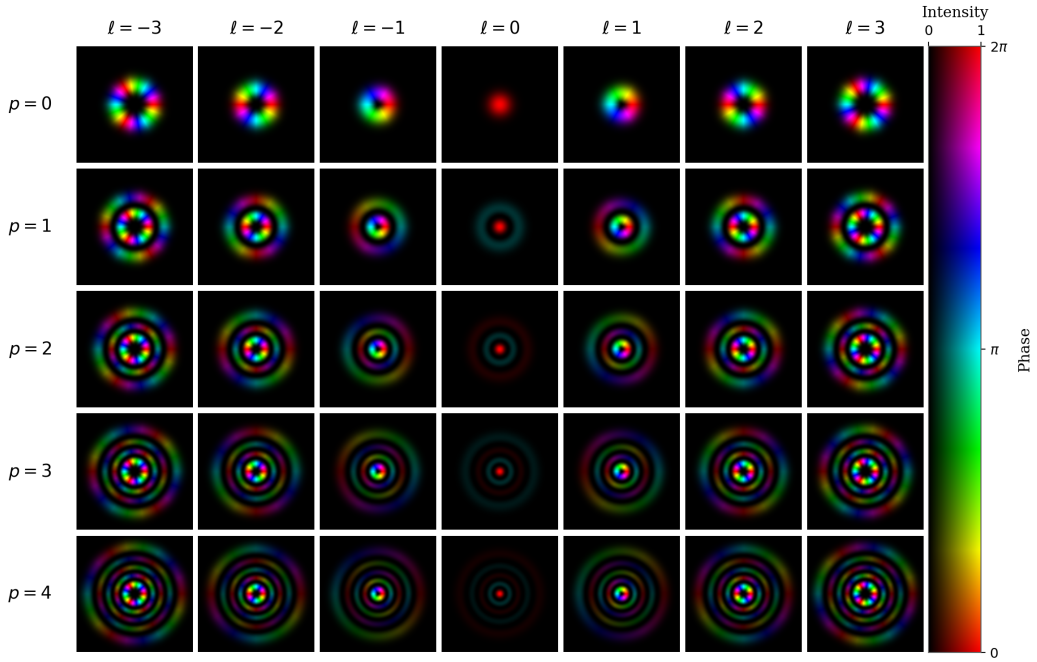


Figure 1.4.2 Laguerre-Gaussian $\mathrm{LG}_{\ell,p}$ modes for varying azimuthal index ℓ (columns) and radial index p (rows).

1.5.2 Temporal Degree of Freedom

As a result of the photon being a localized excitation of the field, the time at which it arrives is itself a degree of freedom. If the arrival window is divided into a set of non-overlapping intervals — time bins — then, consequently, a photon occupying one time bin is thus distinguishable from a photon occupying another. If a single photon may be placed

in a coherent superposition of several bins,

$$|\psi\rangle = \sum_{k=1}^{d} c_k |k\rangle. \tag{1.15}$$

where $|k\rangle$ is the photon occupying the k-th time bin and the complex amplitudes satisfy $\sum_k |c_k|^2 = 1$. An unbalanced Mach-Zehnder interferometer splits a pulse into early and late components separated by a fixed delay, and the relative amplitude and phase of those components are set by beam splitters and phase shifters [15]. Because the bins do not overlap in time they are naturally orthogonal, and a photon distributed over d bins spans a d-dimensional state space. Time-bin encoding is robust against the polarization and mode distortions that accumulate over long propagation distances, which has made it a workhorse of fibre-based quantum communication.

1.5.3 Spectral Degree of Freedom

The final degree of freedom, conjugate to a photon's arrival time and linked to it through the Fourier transform, is its frequency. In direct analogy with the time bins above, a photon can be distributed over a set of discrete frequency bins, each having a distinguishable spectral mode.

This is also the degree of freedom behind a technology that touches nearly everyone. Wavelength-division multiplexing (WDM) [16] sends many independent data channels down a single optical fibre, each carried on its own wavelength, and it is this multiplexing

that lets the optical-fibre backbone of the internet — including the submarine cables that carry the great majority of intercontinental traffic — multiply the capacity of each link by orders of magnitude without laying new fibre [17, 16]. The same principle extends to the single-photon level, where frequency-bin encoding provides a high-dimensional alphabet for quantum information that is naturally compatible with this existing fibre infrastructure.

2

Quantum Entanglement and Biphoton States

This chapter develops the theory needed for the experimental chapters. It quantizes the electromagnetic field, introduces entanglement, the states of quantum optics, describes the spontaneous parametric down-conversion (SPDC) process and the biphoton state with its

spatial and temporal correlations, and reviews the quantum imaging configurations used in Chapter 3.

2.1 Field Quantization and Optical Coherence

Optical coherence is characterised by a hierarchy of normally ordered field correlation functions [18]. The first order describes the detection of a single photon. Writing $\hat{E}^{(+)}$ and $\hat{E}^{(-)}$ for the positive- and negative-frequency parts of the field operator, defined explicitly below, the first-order correlation function is

$$G^{(1)}(\mathbf{r}_1, \mathbf{r}_2) = \langle \hat{E}^{(-)}(\mathbf{r}_1) \hat{E}^{(+)}(\mathbf{r}_2) \rangle. \tag{2.1}$$

whose diagonal

$$G^{(1)}(\mathbf{r}) \equiv G^{(1)}(\mathbf{r}, \mathbf{r}) = \langle \hat{E}^{(-)}(\mathbf{r}) \hat{E}^{(+)}(\mathbf{r}) \rangle \ \propto \ I(\mathbf{r}). \tag{2.2}$$

is the mean photon flux density at $\mathbf{r}$, the quantity accumulated by an intensity-recording detector. Throughout Chapter 3, and following the notation of the manuscript reproduced there, the singles image is denoted $g^{(1)}$. It is the distribution of all single-photon detection events registered on the camera, with no coincidence gating applied, and it is related to the first-order correlation function through

$$g^{(1)}(\mathbf{r}) = \frac{G^{(1)}(\mathbf{r})}{\max_{\mathbf{r}'} G^{(1)}(\mathbf{r}')}. \tag{2.3}$$

that is, the diagonal of the first-order correlation function normalized to its maximum. The superscript records the order of the correlation: a first-order measurement involves a single detection event, whereas the second-order coincidence images Γ_s and Γ_{post} introduced in Chapter 3 involve two photons. The singles image should not be confused with the normalized temporal coherence $g^{(1)}(\tau) = G^{(1)}(\tau)/G^{(1)}(0)$ [cf. Eq. (4.1) of Ref. [18]] obtained by scanning the delay of an interferometer; no such measurement is performed in this work.

The second-order correlation function is the central observable of correlation imaging [18, 20]. The use of intensity correlations to probe light dates back to the seminal stellar interferometry of Hanbury Brown and Twiss [19]. In Glauber's analysis of photon coincidence detection, the rate at which two ideal detectors at transverse positions $\mathbf{r}_1$ and $\mathbf{r}_2$ register photons in coincidence is proportional to the normally ordered field average [Eq. (2.17) of Ref. [18]]

$$G^{(2)}(\mathbf{r}_1, \mathbf{r}_2) = \langle \hat{E}^{(-)}(\mathbf{r}_1)\hat{E}^{(-)}(\mathbf{r}_2)\hat{E}^{(+)}(\mathbf{r}_2)\hat{E}^{(+)}(\mathbf{r}_1)\rangle. \tag{2.4}$$

evaluated here at equal times.[1] This joint detection rate is the quantity recorded experimentally, and for a two-photon state it is fixed by the biphoton amplitude:

$$\Gamma(\mathbf{x}_i, \mathbf{x}_s) \;\equiv\; G^{(2)}(\mathbf{x}_i, \mathbf{x}_s) \;\propto\; |\psi(\mathbf{x}_i, \mathbf{x}_s)|^2, \qquad \psi(\mathbf{x}_i, \mathbf{x}_s) = \langle 0|\, \hat{E}^{(+)}(\mathbf{x}_s)\hat{E}^{(+)}(\mathbf{x}_i)\,|\Psi\rangle. \tag{2.5}$$

[1] Glauber's general definition [Eq. (3.7) of Ref. [18]] carries four independent spacetime arguments; the form above is its specialization to the arguments actually measured in coincidence detection [Eq. (2.17) of the same reference], evaluated at equal times. In the experiments of Chapter 3 the detection is integrated over a coincidence window of 10 ns, far longer than the biphoton correlation time, so the temporal dependence is traced out by the measurement and only the spatial arguments survive. The temporal correlation is used solely as a gate to reject uncorrelated background, not as a scanned variable.

Normalising by the singles rates at the two detection points, in the manner of Eq. (4.3) of Ref. [18], gives the dimensionless

$$g^{(2)}(\mathbf{r}_1, \mathbf{r}_2) = \frac{G^{(2)}(\mathbf{r}_1, \mathbf{r}_2)}{G^{(1)}(\mathbf{r}_1)\, G^{(1)}(\mathbf{r}_2)}. \tag{2.6}$$

which measures the degree of correlation between the two detection events relative to statistically independent detections: $g^{(2)} = 1$ for uncorrelated events, and $g^{(2)} > 1$ where joint detections are enhanced. For spatially entangled pairs from spontaneous parametric down-conversion [21, 22], Γ is strongly peaked when the detected coordinates satisfy the source correlation and falls away from it. This correlation structure acts as the primary physical resource exploited to extract image information from coincidence measurements, as first demonstrated in two-photon ("ghost") imaging [6].

For spatially entangled photon pairs, typically generated through spontaneous parametric down-conversion [21, 22], $g^{(2)}$ is strongly peaked for correlated detection events and approaches unity for uncorrelated positions. This distinct correlation structure acts as the primary physical resource exploited to extract image information from coincidence measurements, as first demonstrated in two-photon ("ghost") imaging [6].

The correlation functions and two-photon states are written in terms of field operators whose explicit mathematical meanings are established in this section. The classical electromagnetic field is quantized by expanding it in a complete set of modes labeled by wave vector $\mathbf{k}$ and polarization σ, and promoting each mode amplitude to an operator

[20, 23, 24]:

$$\hat{E}(\mathbf{r},t) = \sum_{\mathbf{k},\sigma} \sqrt{\frac{\hbar\omega_{\mathbf{k}}}{2\varepsilon_0 V}} \boldsymbol{\varepsilon}_{\mathbf{k}\sigma} \left(a_{\mathbf{k}\sigma} e^{i(\mathbf{k}\cdot\mathbf{r}-\omega_{\mathbf{k}}t)} + a^{\dagger}_{\mathbf{k}\sigma} e^{-i(\mathbf{k}\cdot\mathbf{r}-\omega_{\mathbf{k}}t)} \right). \tag{2.7}$$

where $\boldsymbol{\varepsilon}_{\mathbf{k}\sigma}$ represents the polarization unit vector and V denotes the quantization volume. The creation ($a^{\dagger}_{\mathbf{k}\sigma}$) and annihilation ($a_{\mathbf{k}\sigma}$) operators add and remove one quantum of excitation—one photon—from a given mode, and obey the fundamental bosonic commutation relation [23, 24]:

$$[a_{\mathbf{k}\sigma}, a^{\dagger}_{\mathbf{k}'\sigma'}] = \delta_{\mathbf{k}\mathbf{k}'}\delta_{\sigma\sigma'}. \tag{2.8}$$

The eigenstates of the number operator $n_{\mathbf{k}\sigma} = a^{\dagger}_{\mathbf{k}\sigma} a_{\mathbf{k}\sigma}$ form the Fock (number) state basis $|n_{\mathbf{k}\sigma}\rangle$ [24], with $a_{\mathbf{k}\sigma}|n_{\mathbf{k}\sigma}\rangle = \sqrt{n_{\mathbf{k}\sigma}}|n_{\mathbf{k}\sigma}-1\rangle$ and the vacuum state defined by $a_{\mathbf{k}\sigma}|0\rangle = 0$. The single- and two-photon Fock states are uniquely relevant for correlation imaging applications. The two-photon amplitude, written later as $\Psi(\mathbf{r}_1, \mathbf{r}_2)$, is precisely a matrix element of these field operators evaluated between the two-photon state and the vacuum.

In contrast, a second critical class of states consists of the coherent states $|\alpha_{\mathbf{k}\sigma}\rangle$ [25, 26], which are eigenstates of the annihilation operator such that $a_{\mathbf{k}\sigma}|\alpha_{\mathbf{k}\sigma}\rangle = \alpha_{\mathbf{k}\sigma}|\alpha_{\mathbf{k}\sigma}\rangle$ [23]. These states describe the output of an ideal laser and serve as the classical benchmark against which the quantum advantage of entangled-photon imaging is rigorously measured.

2.2 Entanglement and Quantum States

The quantum description of light permits the existence of states that have no classical analogue. The most important, of which this thesis concentrates on, is entanglement. The quantum description of entanglement follows: a state of two or more photons that cannot be written as a product of individual single-photon states [24]. For two photons labelled signal (s) and idler (i), a separable state takes the product form:

$$|\Psi\rangle = |\psi\rangle_s \otimes |\psi\rangle_i. \tag{2.9}$$

with each photon in a definite state of its own.

Entangled states do not permit such factorization. The canonical examples of entangled states are the four polarization Bell states [20, 24, 27],

$$|\Phi^{\pm}\rangle = \frac{1}{\sqrt{2}} \left(|H\rangle_s |H\rangle_i \pm |V\rangle_s |V\rangle_i \right), \tag{2.10}$$

$$|\Psi^{\pm}\rangle = \frac{1}{\sqrt{2}} \left(|H\rangle_s |V\rangle_i \pm |V\rangle_s |H\rangle_i \right). \tag{2.11}$$

each a superposition of two product terms that cannot be factored into a single product versions of $|\psi\rangle_s \otimes |\psi\rangle_i$. Neither photon carries a polarization of its own before measurement, yet the two outcomes are perfectly correlated (anti-correlated). The consequence is that a measurement of the signal photon in the basis $\{|H\rangle, |V\rangle\}$ immediately fixes the result for the idler photon. The four Bell states, moreover, are mutually orthogonal and normalized,

and therefore together they span the four-dimensional Hilbert space of the two photons' joint polarization.

2.3 Spontaneous Parametric Down-Conversion

Spontaneous parametric down-conversion (SPDC) is the second-order nonlinear optical process ($\chi^{(2)}$) used in this thesis to generate the photon pairs required for correlation imaging [22, 28]. In SPDC, a pump photon is converted probabilistically inside a nonlinear crystal into two lower-energy photons, conventionally labelled signal and idler [29, 30]. For the present work, the importance of SPDC is not simply that it produces pairs of photons, but that the spatial and spectral structure of the generated two-photon state is a direct product of both the pump field and the phase-matching conditions of the nonlinear ($\chi^{(2)}$) crystal [31]. Those source properties determine the correlations that are later exploited to improve image recovery in the presence of scattering.

The SPDC process is first constrained by energy conservation [28],

$$\omega_p = \omega_s + \omega_i. \tag{2.12}$$

where ω_p, ω_s, and ω_i denote the angular frequencies of the pump, signal, and idler fields, respectively. In the degenerate situation, the two down-converted photons share the pump energy equally, such that $\omega_s = \omega_i = \omega_p/2$. Efficient SPDC also requires momentum

conservation, expressed as the phase-matching condition [28]:

$$\vec{k}_p = \vec{k}_s + \vec{k}_i. \tag{2.13}$$

Realistically, this condition within the nonlinear crystal is satisfied only within a finite bandwidth, so it is more useful to work in terms of a phase mismatch. Decomposing the mismatch into longitudinal and transverse components gives [28]

$$\Delta k_z = k_{p,z} - k_{s,z} - k_{i,z}, \tag{2.14}$$

$$\Delta \vec{k}_\perp = \vec{k}_{p,\perp} - \vec{k}_{s,\perp} - \vec{k}_{i,\perp}. \tag{2.15}$$

This decomposition is physically important for imaging. The mismatch condition for the longitudinal component governs how phase accumulates across the finite crystal length and, therefore, controls the phase-matching bandwidth. The mismatch condition for the transverse component, however, determines which emission angles and transverse momenta are efficiently generated. Together, they fix the angular distribution of the photon pairs and therefore the spatial mode structure available to the imaging system.

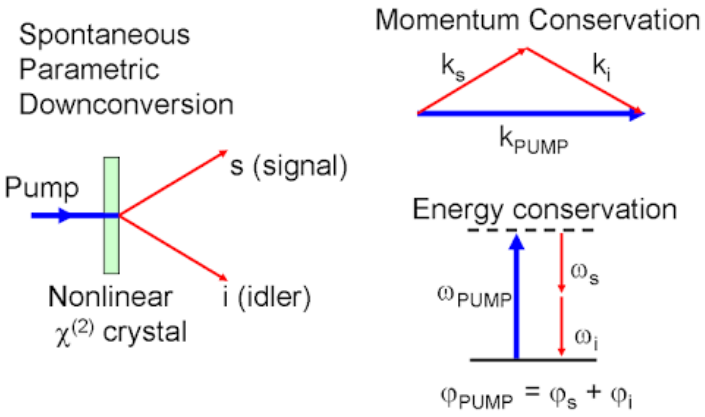


Figure 2.1. Spontaneous Parametric Down-Conversion (SPDC) process. A pump photon incident on a second-order nonlinear ($\chi^{(2)}$) crystal spontaneously splits into two lower-energy photons, the signal and idler. The process conserves energy, $\omega_p = \omega_s + \omega_i$, and momentum, $k_p = k_s + k_i$ (the phase-matching condition). Figure from [32].

Birefringent phase matching in a uniaxial crystal admits two polarization configurations, conventionally labelled Type-I and Type-II [33, 34]. In Type-I phase matching, the signal and idler are generated with identical polarization, defined as orthogonal to that of the pump polarization; in a negative uniaxial crystal, this corresponds to an extraordinary-polarized pump decaying into two ordinary-polarized photons, $e \to o + o$. In Type-II phase matching, the pair carries mutually orthogonal polarizations, one ordinary and one extraordinary, $e \to o + e$. The specific configuration realized is determined by the combination of ordinary and extraordinary refractive indices that satisfies the phase-matching condition $\vec{k}_p = \vec{k}_s + \vec{k}_i$, and is tuned in practice through the orientation of the crystal's optic axis and its temperature. This distinction changes both the accessible phase-matching geometry and the method used to separate the two photons after the crystal. Type-I sources are

attractive when brightness and symmetric spatial structure are prioritized, whereas Type-II sources provide a natural polarization label that simplifies routing into distinct optical arms, at the cost of additional birefringent walk-off and temporal mismatch [35].

A second distinction is between the collinear and non-collinear emission geometries [22]. In collinear SPDC, signal and idler photons propagate approximately along the pump axis; in non-collinear SPDC, they emerge at distinct angles set by the crystal and phase-matching condition. For imaging systems, non-collinear operation is advantageous, as it provides a direct geometrical separation between the two photons, making it easier to send one through the object or scattering channel while directing its partner to a reference arm, and it eases the burden on downstream optics for pump rejection and path separation.

SPDC is an intrinsically low-efficiency process, operated in the low-gain regime [30]. The usable operating point is set by a trade-off between coincidence yield and the onset of multi-pair emission, which acts as a background in correlation measurements. Common nonlinear media include beta-barium borate (BBO), potassium titanyl phosphate (KTP), and periodically poled KTP (PPKTP); BBO remains a standard bulk crystal for birefringent phase matching, while KTP-based materials are attractive when stronger nonlinearity or quasi-phase matching is desired. In all cases, crystal choice, crystal length, pump focusing, filtering, and collection geometry jointly determine the brightness and mode structure delivered to the experiment.

2.4 The Biphoton State and its Correlations

A useful starting point for the spatial description is the Type-I two-photon detection amplitude derived for a monochromatic pump [22]. Under quasi-collinear, frequency-degenerate conditions, and in the thin-crystal limit where the longitudinal phase-matching envelope is broad over the relevant transverse-momentum range, the two-photon amplitude reduces to the compact form

$$\Phi(\vec{q}_s, \vec{q}_i) \propto v(\vec{q}_s + \vec{q}_i)\,\mathrm{sinc}(\Delta k_z L/2)\,. \tag{2.16}$$

where $\vec{q}_s$ and $\vec{q}_i$ are the transverse wave vectors of the signal and idler, L is the crystal length, $v(\vec{q}_s + \vec{q}_i)$ is the pump angular spectrum, and the sinc term encodes the finite phase-matching bandwidth. This expression is central for imaging: the pump structure is transferred to the biphoton state through the sum coordinate $\vec{q}_s + \vec{q}_i$, while the crystal length limits the allowed transverse-momentum bandwidth through the phase-matching term [36]. A thinner crystal broadens the phase-matching envelope and allows the pump profile to be mapped more directly onto the generated two-photon field.

The coincidence detection rate between detectors at positions $\mathbf{r}_1$ and $\mathbf{r}_2$ is proportional to the joint detection probability. For a two-photon state $|\Psi\rangle$,

$$R_c(\vec{r}_1, \vec{r}_2) \propto \iint d\vec{r}\,'_1\, d\vec{r}\,'_2\, \left|\langle 0|\hat{E}(\vec{r}_2)\hat{E}(\vec{r}_1)|\Psi\rangle\right|^2 T(\vec{r}\,'_1)\, D_1(\vec{r}_1, \vec{r}\,'_1)\, D_2(\vec{r}_2, \vec{r}\,'_2). \tag{2.17}$$

where $T(\vec{r})$ is the object transmission function placed in one arm and D_1, D_2 describe the

efficiency and spatial resolution of the two detectors. The image is reconstructed from the dependence of R_c on detector position. The two-photon state generated by Type-I SPDC in the thin-crystal approximation can be written in the transverse position representation as

$$|\Psi\rangle = \iint d\vec{r}_s \, d\vec{r}_i \; \phi(\vec{r}_s, \vec{r}_i) \; \hat{a}_s^\dagger(\vec{r}_s) \, \hat{a}_i^\dagger(\vec{r}_i) \, |0\rangle. \tag{2.18}$$

where $\hat{a}_s^\dagger$ and $\hat{a}_i^\dagger$ create signal and idler photons at transverse positions $\vec{r}_s$ and $\vec{r}_i$, and $\phi(\vec{r}_s, \vec{r}_i)$ is the two-photon amplitude [31]. In the near field at the crystal output plane, transverse momentum conservation produces a tight position correlation,

$$\phi(\vec{r}_s, \vec{r}_i) \approx \delta(\vec{r}_s - \vec{r}_i) \, f(\vec{r}_s). \tag{2.19}$$

where $f(\vec{r}_s)$ is the pump beam profile: if the signal photon is detected at $\vec{r}_s$, the idler is found at the same transverse position, and the correlation directly maps the pump shape [35, 37]. In the far field, obtained by Fourier transforming the near-field amplitude, the structure becomes a momentum anti-correlation,

$$\tilde{\phi}(\vec{q}_s, \vec{q}_i) \approx \delta(\vec{q}_s + \vec{q}_i) \, g(\vec{q}_s). \tag{2.20}$$

with $g(\vec{q}_s)$ determined by the pump angular spectrum. The anti-correlation $\vec{q}_s + \vec{q}_i = 0$ is a direct consequence of transverse momentum conservation. This complementary structure — position correlation in the near field, momentum anti-correlation in the far field — is the signature of Einstein–Podolsky–Rosen entanglement in the spatial degrees of freedom,

and by imaging at different propagation distances one can access whichever balance of correlations a given imaging task requires.

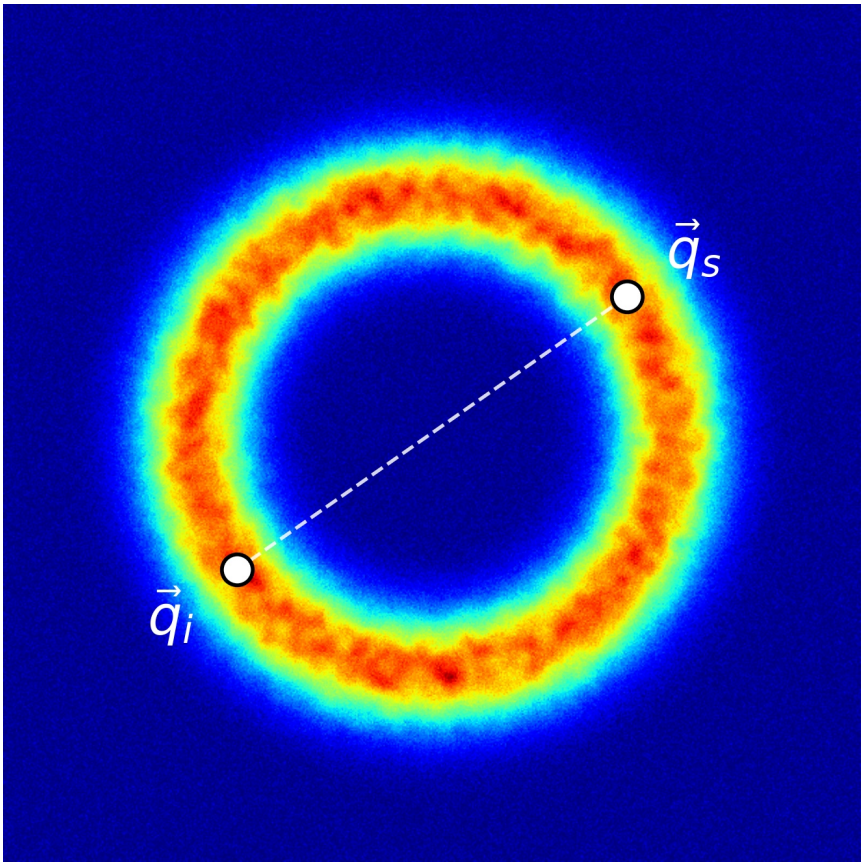


Figure 2.2. Far-field SPDC intensity profile. In the far field, the down-converted photons are anti-correlated in transverse momentum: a signal photon detected at $\vec{q}_s$ *defines* its conjugate pair at the opposite point $\vec{q}_i = -\vec{q}_s$ due to momentum conservation.

The strength and dimensionality of the spatial entanglement are quantified by the

Schmidt decomposition of the two-photon state [36],

$$|\Psi\rangle = \sum_k \sqrt{\lambda_k}\, |\phi_k\rangle_s\, |\chi_k\rangle_i. \tag{2.21}$$

where the λ_k are Schmidt coefficients satisfying $\sum_k \lambda_k = 1$, and $|\phi_k\rangle_s$, $|\chi_k\rangle_i$ form orthonormal bases for the signal and idler. The Schmidt number,

$$K = \frac{1}{\sum_k \lambda_k^2}. \tag{2.22}$$

quantifies the effective number of entangled modes: $K = 1$ corresponds to a separable state, and larger values indicate stronger high-dimensional entanglement [31]. For SPDC in the thin-crystal limit with a Gaussian pump, K is set by the ratio of the pump beam size to the crystal-determined correlation length, so a larger pump or thinner crystal yields higher-dimensional entanglement and, in turn, improved imaging resolution and field of view.

Temporal correlations arise from energy conservation and the process's finite bandwidth. Photon pairs are created simultaneously within the coherence time of the pump, which is inversely related to the pump bandwidth; for a narrow-band pump, the signal and idler are strongly correlated in time, with correlation times ranging from below a picosecond to nanoseconds depending on the applied spectral filtering [36]. Two distinct time scales must not be conflated here. The biphoton correlation time is a property of the state: the width of the joint temporal amplitude of the pair, set by the phase matching and the

spectral filtering; for the 10 nm filters at 810 nm used in Chapter 3 it is of order ≈ 0.2 ps. The coincidence window τ_c is a property of the apparatus: the interval within which two detection events are registered as a pair, set in practice by the 7 ns timing resolution of the camera and chosen in Chapter 3 as 10 ns. The window exceeds the correlation time by about five orders of magnitude, so every true pair falls comfortably inside it; its size does not determine whether pairs are found, but how much uncorrelated background is accepted, with the accidental rate increasing in proportion to τ_c. These temporal and spatial correlations are precisely the resource that enables background rejection when imaging through a scattering medium; how these correlations evolve and degrade as they pass through such a medium is explored quantitatively in Chapter 3.

2.5 Quantum Imaging with Biphotons

The correlations derived above can be turned into images in several configurations. The foundational demonstration was ghost imaging [6], in which the photon pairs are divided into two paths, one photon passes through the object while the other photon from the pair travels to a spatially resolving detector that never views the object. The image is reconstructed from the pattern of coincidences between the two detectors rather than from either detector alone. Because only correlated pairs contribute to the coincidence signal, uncorrelated background photons — from ambient light, detector dark counts, or scattered radiation — are suppressed or rejected, providing contrast enhancement in high-noise environments where conventional single-detector imaging might fail.

In biphoton, or coincidence, imaging, the object information is encoded in the second-order correlation function $G^{(2)}$ rather than in the mean intensity, and the imaging system is designed such that the spatial correlation of the source matches the numerical aperture, magnification, and mode structure of the optics. The shared feature between these imaging configurations is correlation-based filtering or post-selection: by accepting only light that arrives in correlated pairs, the system intrinsically rejects diffuse, uncorrelated light and thereby enhances contrast. It is this principle, applied to propagation through weakly scattering media, that the experiment of Chapter 3 develops and demonstrates.

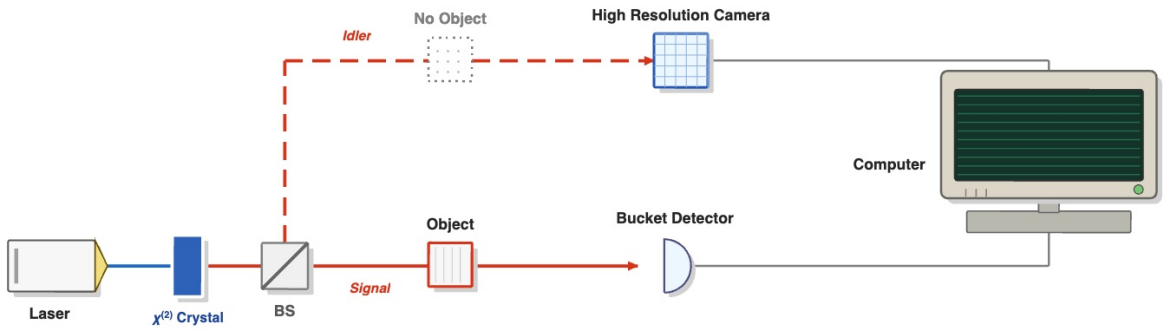


Figure 2.3. Schematic for Ghost Imaging. Photon pairs generated by spontaneous parametric down-conversion are separated into two arms; the signal photon interacts with an object and afterwards is collected by a single-pixel ("bucket") detector with no spatial resolution, meanwhile the idler photon, which never interacts with the object and is incident uninterruptedly onto a spatially-resolving detector or camera. The imaging systems are not shown in the sketch.

3

Entanglement-Enhanced Imaging in Scattering Environments

This chapter is based on the following preprint:

A. D'Errico, J. Hubble, R. Abolhassani, N. Dehghan, Y. Klein, Y. Zhang, and E. Karimi, *"Contrast-enhanced imaging through weakly scattering media with spatially entangled pho-*

tons," arXiv:2605.28998 (2026).

A. D'Errico and Y. Klein conceived the project. A. D'Errico developed the simulation framework. J. Hubble, R. Abolhassani, N. Dehghan, and A. D'Errico, with contributions from Y. Klein and Y. Zhang, designed and assembled the experimental apparatus and performed the measurements. Y. Zhang developed the software for extracting post-selected correlation images, with contributions from A. D'Errico. A. D'Errico, Y. Klein, J. Hubble, and R. Abolhassani analyzed the data. The manuscript was initially drafted by A. D'Errico, J. Hubble, and R. Abolhassani. E. Karimi supervised the research and provided overall guidance throughout the project.

3.1 Scattering Media

Imaging techniques — from microscopy and light detection and ranging to astronomy — can be degraded by unknown inhomogeneities in the medium between the source and the detector, with the loss of quality expressed as reduced resolution, reduced contrast, or both. Whether the medium is a turbulent atmosphere, fog, a multimode waveguide, or biological tissue, propagation is altered by phase aberrations, scattering, and loss of coherence. The common challenge, shared by classical and quantum optical imaging alike, is to devise techniques that counter these undesired effects and recover image quality. Existing approaches fall into a few broad families: *filtering* techniques, which isolate the components of the

light field that still carry residual information about the object; *numerical* methods, which use knowledge of the physical properties of the medium to recover effective point-spread functions; and *correction* methods, in which the medium is experimentally characterized — for instance through its transmission matrix — and its effect compensated with a spatial light modulator.

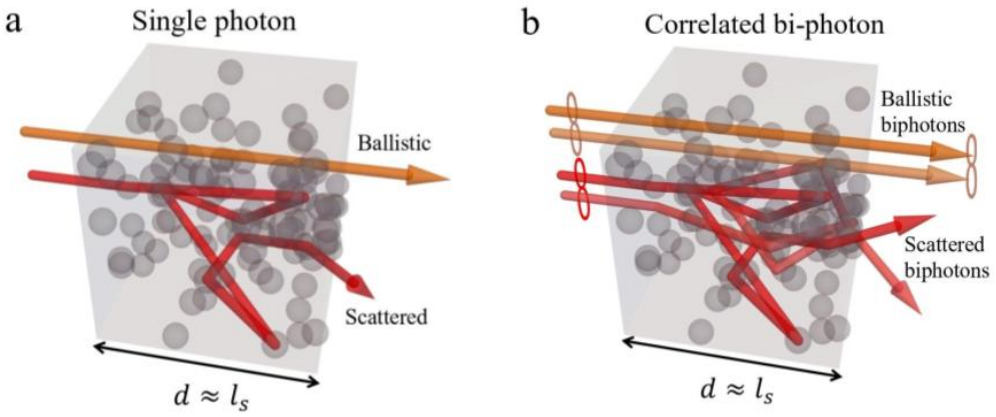


Figure 3.1. Conceptual Illustration of Scattering Media. In weakly scattering media (thickness d no greater than a few times the mean free path ℓ_s), ballistic light can be separated from scattered light. Ballistic photons carry the image; ballistic biphotons additionally preserve their spatial entanglement, allowing scattered pairs to be removed by correlation post-selection.

The extension of these strategies to the few-photon regime is driven by the growing reach of quantum imaging, which exploits entangled two-photon states and spatially resolved coincidence detection. Two-photon correlations in different degrees of freedom have been

studied extensively in complex media, revealing the migration of entanglement into specific sets of scattering modes, characteristic features in the resulting correlation speckles, the survival of polarization entanglement through tissue, and enhanced effects such as the coherent back-scattering of entangled pairs; spatiotemporal correlations have likewise been turned into adaptive-optics schemes that operate directly at the single-photon level.

In classical optics, filtering works by distinguishing and isolating the different paths light takes through the medium. One separates *ballistic* photons, which propagate essentially undisturbed and still carry a faithful picture of whatever lies beyond, from *scattered* photons, whose optical paths are modified one or more times by scattering centres and which arrive carrying no picture of anything; photons whose paths are only weakly perturbed relative to the ballistic ones are termed "snake" photons. Such filtering is effective only in the *weakly scattering* regime, where the medium thickness d is at most of order the mean scattering length ℓ_s — in practice $d \lesssim 5\,\ell_s$ — so that the ballistic contribution remains significant. Under pulsed illumination, scattered light can be rejected by time gating, which exploits the fact that ballistic photons are the first to reach the detector; under continuous-wave illumination, spatial or coherence filtering is used instead; and either may be combined with polarization filtering, since scattered photons can accumulate a polarization different from that of the input radiation.

It is useful to describe the action of the medium on the field directly. A thin object or layer is represented by a complex transmission function

$$t(x, y) = a(x, y)\, e^{i\phi(x,y)}. \tag{3.1}$$

with an amplitude term $a(x, y)$ and a phase term $\phi(x, y)$. For a transparent or semi-transparent medium the amplitude is simply attenuated, $a(x, y) < 1$; for a medium that is principally refractive the amplitude is left essentially unchanged and the field instead acquires a spatially varying phase, set by the local optical path length — a variation in thickness or in refractive index across x and y imprints a corresponding phase $\phi(x, y)$, so that a medium of varying thickness scatters the phase with a defined transverse profile. In thin scattering media this phase scrambling is the dominant effect: scattering manifests as transversely varying random phase shifts rather than amplitude loss, which is precisely why such media can be emulated experimentally by random phase masks placed in planes conjugate to the object.

This is also exactly the regime in which the conventional rejection strategies above become ineffective or impractical. Time gating demands ultrashort pulses or broadband light of very low coherence length, because the temporal delay a thin layer imposes on scattered light is too small to resolve; polarization filtering offers little benefit in the absence of significant anisotropy; and spatial filtering rejects scattered light only at the cost of resolution. Yet even a thin scattering layer can substantially reduce image contrast, so an alternative means of discriminating ballistic from scattered light is required.

Here, we address this problem using spatially entangled photon pairs as the illumination source. The approach exploits the fact that propagation through a scattering medium degrades the spatial correlations between entangled photons, whereas pairs that follow ballistic or near-ballistic, "snake"-like paths can largely preserve their initial correlations. The object is imaged with spatially entangled photons, and coincidences are recorded with

their transverse positions resolved: ballistic biphotons retain the source correlation, so their detected coordinates remain related by $x_i \approx x_s + \xi$ and populate the diagonal of the spatial-correlation matrix, while scattered biphotons lose this relation and spread to off-diagonal events. By post-selecting only the coincidences whose detected transverse coordinates remain consistent with the correlations present before propagation, we suppress the scattered-biphoton contribution and preferentially retain ballistic pairs, enhancing contrast relative to a single-photon detection strategy. The temporal correlation acts in concert: because only photons arriving within a narrow coincidence window are counted, uncorrelated background — ambient light, detector dark counts, and stray scattered photons from other pairs — is strongly suppressed at the same time. Combining temporal coincidence detection with spatial post-selection on the quantum correlations in this way enhances the imaging contrast of objects embedded in weakly scattering media; Sections 3.2 and 3.3 quantify the improvement through the modulation transfer function, finding gains of up to roughly three-fold over non-post-selected coincidences and five-fold over classical single-photon imaging.

Chapter 2 derived the complementary structure of the spatial entanglement in two Fourier-related planes: in the **near field**—any plane in which the crystal is imaged—the two photons are correlated in position, being found at the same transverse location, while in the **far field**—any plane in which the Fourier transform of the source plane is formed, such as the focal plane of a lens—they are anti-correlated in transverse momentum, and are therefore found at opposite positions with respect to the beam axis (Figure 2.2). These two planes play distinct roles in the experiment. The scattering screens act in far-field planes,

where the pair is anti-correlated: the two photons of a pair strike the random mask at separated, roughly opposite points, and so acquire independent random phases whenever their separation exceeds the phase correlation width w_A of the mask—the origin of the scattering-strength criterion w_q/w_A defined in Section 3.2. Detection, by contrast, takes place in the near field: the camera sits in an image plane of the crystal and of the object, where a ballistic pair—one whose photons traversed the masks without being scattered—still arrives position-correlated, $\mathbf{x}_i \approx \mathbf{x}_s$, while a scattered pair does not. The post-selection $\mathbf{x}_i \approx \mathbf{x}_s + \boldsymbol{\xi}$ therefore tests, pair by pair, for the near-field correlation that only the ballistic subset preserves.

3.2 Biphoton Imaging

Spatially correlated pairs are generated by spontaneous parametric down-conversion in a $1,\mathrm{mm}$-thick Type-I β-barium borate (BBO) crystal pumped by a pulsed $405,\mathrm{nm}$ laser; the frequency-degenerate photons at $810,\mathrm{nm}$ are selected with $10,\mathrm{nm}$ bandpass filters. A relay-imaging system re-images the crystal plane onto the object location, where the two photons overlap, while in the far field, the pair is spatially anti-correlated so that each photon samples a different region of the scattering screens. Two reflective liquid-crystal spatial light modulators (SLM1 and SLM2) introduce the random phase patterns that play the roles of the scattering planes S_1 (before the object) and S_2 (after it). These are $S1$ and $S2$, which are located in the Fourier plane before and after the object, respectively. Signal and idler are probabilistically separated into two optical paths and imaged onto two

regions of a time-stamping camera (Tpx3Cam) fitted with an image intensifier; the camera records the position and arrival time of each detected event with nanosecond resolution. Coincidences are identified in post-processing by retaining pairs of detections that occur within a 10 ns coincidence window.

Accidental coincidences are pairs of detections that satisfy the temporal coincidence condition but do not originate from the same SPDC pair. They can arise from photons belonging to different pair-generation events, from background or detector events, or when one photon of a generated pair is lost through finite optical transmission or detection efficiency and the detected photon is then paired with an unrelated event. The probability of such accidental associations increases with the measured singles rates in the two detection regions and with the width of the coincidence window. The $10,\mathrm{ns}$ temporal window therefore suppresses accidental coincidences by restricting the interval over which unrelated detections may be associated, but it does not remove those that fall within the accepted window. No explicit accidental-coincidence or detector-background subtraction is applied to the coincidence images reported here; residual accidentals remain in the measured coincidence distribution and are further suppressed by the subsequent spatial post-selection.

The object imaged throughout this section is a simple amplitude target: three dark lines drawn with a black marker on a fragment of transparent plastic, placed in the image plane of the crystal. Its appearance on the camera in the absence of scattering, which features three dark stripes on a bright background, serves as the ground truth against which all reconstructions are compared.

The scattering strength quoted throughout this chapter is the ratio w_q/w_A, where w_q is the width of the far-field anti-correlation of the pair (set by the phase matching, Chapter 2) and w_A is the width of the disorder-averaged autocorrelation of the random phase masks. For $w_q < w_A$, the two photons of a pair sample essentially the same phase and their correlation survives; for $w_q > w_A$, each photon in the pair, on average, acquires an independent random phase and the near-field correlation broadens. Experimentally, w_q/w_A is estimated from this broadening: the near-field correlation width is measured with (w_-) and without ($w_{-,0} = 2/w_q$) the scattering masks applied, and the measured ratio is inverted through the semiempirical relation

$$\frac{w_-}{w_{-,0}} = \sqrt{1 + 3\left(\frac{w_q}{w_A}\right)^2}, \tag{3.2}$$

obtained from numerical simulations of the biphoton propagation; in the correlation-imaging configuration, where only one photon is scattered, the relation is corrected to

$$\frac{w_-}{w_{-,0}} = \sqrt{\frac{1 + 3\left(\frac{w_q}{w_A}\right)^2}{2}}. \tag{3.3}$$

The estimate agrees qualitatively with a direct comparison between the phase-matching intensity measured on the SLM plane and the applied holograms.

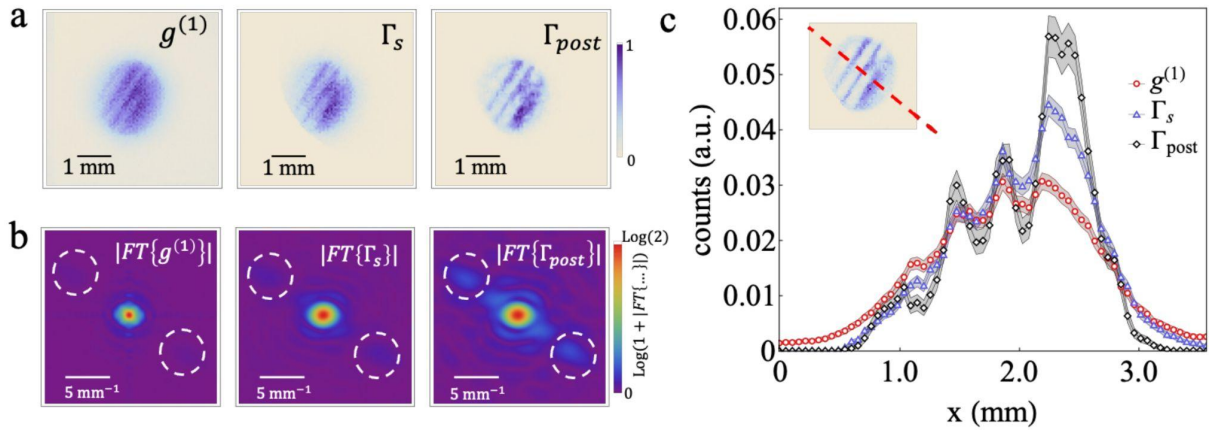


Figure 3.2. Contrast enhancement with static scattering medium between object and camera ($w_q/w_A \approx 3.4$). A single, fixed random phase mask is applied on SLM2, between the object and the detector; no scattering acts before the object, so the strong spatial correlations are preserved on the object plane. Post-selected coincidences reveal the object features with markedly enhanced contrast relative to both the singles image ($g^{(1)}$) and the non-post-selected coincidence image (Γ_s); a contrast enhancement is already visible in Γ_s, since the two photons are correlated on the object plane. From the Fourier spectra, the MTF is estimated at 3.05% ($g^{(1)}$), 5.3% (Γ_s), 15.6% ($\Gamma^{(3)}_{post}$).

The detected coincidence distribution is $\Gamma(x_i, x_s) \propto |\psi(x_i, x_s)|^2$ in the source/object image plane. An ordinary coincidence image is the marginal $\Gamma_s(x_s) = \sum_{x_i} \Gamma(x_i, x_s)$; in the presence of scattering, its contrast is strongly reduced, because most scattered pairs fall off the diagonal while ballistic pairs concentrate on it. The post-selected image keeps only the diagonal band,

$$\Gamma_{post}(x; \xi) := \Gamma(x_i = x_s + \xi). \tag{3.4}$$

which preferentially retains the ballistic biphotons while rejecting scattered pairs. This causes far fewer events to survive the post-selection process, and for Γ_{post} to carry higher

shot noise. The noise can be recovered without discarding the contrast by noting that different offsets ξ produce only a rigid translation of the same post-selected image; summing $n \times n$ appropriately shifted images,

$$\Gamma^{(n)}_{post}(x) = \sum_{\xi_x,\xi_y=1,\ldots,n} \Gamma_{post}(x-\xi,\xi). \tag{3.5}$$

increases the event count while preserving the enhancement. There is consequently a trade-off in the choice of n — larger n improves the signal-to-noise ratio but gradually dilutes the contrast — and an optimal value lies in between.

Before turning to the results, it is worth stating why three reconstructions are compared. The singles image $g^{(1)}$ is the classical benchmark: it is what any intensity-recording camera would measure, and each claimed enhancement must be measured against it. The coincidence image Γ_s isolates the effect of the temporal correlation alone. For a pure two-photon state detected with unit efficiency and no background, the two would be identical. This occurs because the marginal of the joint distribution reproduces the singles distribution exactly,

$$\Gamma_s(\mathbf{x}_s) = \sum_{\mathbf{x}_i} \Gamma(\mathbf{x}_i,\mathbf{x}_s) \;\propto\; \int d\mathbf{x}_i \, |\psi(\mathbf{x}_i,\mathbf{x}_s)|^2 = \; G^{(1)}(\mathbf{x}_s). \tag{3.6}$$

Experimentally they differ, because the singles additionally register events with no detected partner: residual background light, detector dark counts, and photons whose twin was lost to absorption or finite detection efficiency. Coincidence gating removes this

uncorrelated contribution, and that is the origin of the modest improvement of Γ_s over $g^{(1)}$. The improvement is only modest because the temporal gate rejects uncorrelated light but not scattered biphotons, which remain correlated in time and continue to contribute to Γ_s. Separating those requires a second, independent filter acting on the spatial correlation—the post-selection $\xi = x_{\mathbf{s}} + \dots$ defined above. The three images therefore form a controlled comparison: $g^{(1)}$ sets the classical baseline, Γ_s adds the temporal filter, and Γ_{post} adds the spatial one. The two filters are complementary (the temporal window suppresses background, while the spatial window suppresses scattering), and the stepwise comparison attributes the observed contrast enhancement to each mechanism separately.

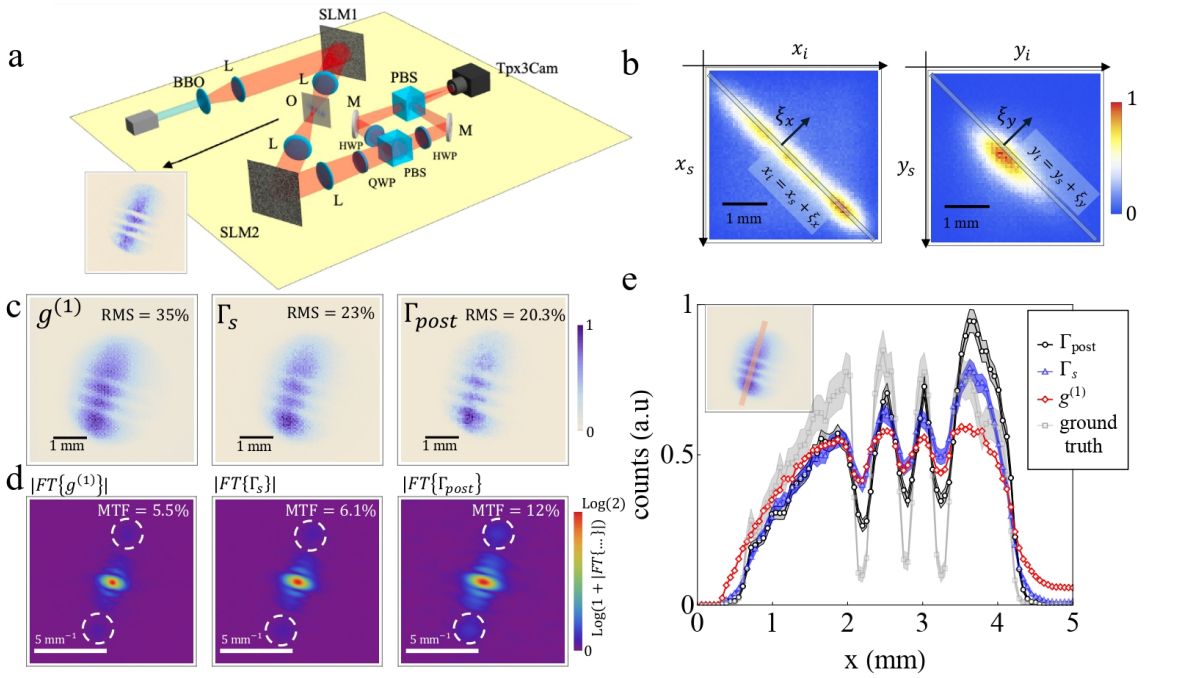


Figure 3.3 Contrast enhancement with dynamic scattering media before and after object ($w_q/w_A \approx 3.4$). Random phase patterns are displayed on SLM1 (before the object) and SLM2 (after the object) and varied over the acquisition, so the recorded coincidences average over several independent scattering realizations. The singles image $g^{(1)}$ and the non-post-selected coincidence image Γ_s show only faint object features, and Γ_s improves only marginally on $g^{(1)}$. The post-selected image $\Gamma^{(6)}_{post}$, by contrast, recovers the line structure clearly. From the Fourier spectra, the MTF is estimated at 5.5% ($g^{(1)}$), 6.1% (Γ_s), and 12% ($\Gamma^{(6)}_{post}$).

Contrast is quantified through a modulation transfer function (MTF), defined as the ratio between the dominant non-zero and the zero spatial-frequency components of the Fourier transform of the recorded image,

$$\mathrm{MTF} = \frac{\max, |FT[I_{\mathrm{scatt}}](k \approx k_0)|,}{\max, |FT[I_{\mathrm{scatt}}](k \approx 0)|,}. \tag{3.7}$$

with k_0 the spatial frequency of the object's periodic structure. From the Fourier spectra, the MTF is estimated at 5.5% for the singles, 6.1% for the coincidences, and 12% for the post-selected coincidences. Thus, post-selection more than doubles the contrast relative to direct imaging and nearly doubles the contrast relative to non-post-selected coincidences. The 1D cross-sections in the same figure confirm that the differences between the three profiles exceed the estimated counting uncertainty. The shaded error bands are calculated assuming Poissonian photon-counting statistics. For each point i in the one-dimensional profile, the counting uncertainty is estimated as $\sqrt{N_i}$, where N_i is the number of detected counts contributing to that point. After normalization by the total number of counts N_{tot} in the corresponding profile, the uncertainty used for the plotted profile is

$$\sigma_i = \frac{\sqrt{N_i}}{N_{\text{tot}}}. \tag{3.8}$$

The shaded bands correspond to $\pm 3\sigma_i$ around each profile value. The quoted MTF values are obtained independently from the Fourier spectra of the reconstructed images.

The two scattering planes play distinct roles, and comparing the dynamic and static cases makes this explicit. The mask S_1, placed between source and object, scrambles the two-photon correlation itself, eroding the advantage that correlated illumination would otherwise provide; the mask S_2, placed between object and detector, reduces image contrast in the same way as it would for ordinary incoherent illumination. For intensity imaging, only S_2 matters, whereas for coincidence imaging, both S_1 and S_2 act. One might therefore expect that introducing S_1 would destroy any benefit of using correlated photons — yet

the dynamic result of Figure 3.3, where both screens are active, shows that this is not so: the surviving ballistic biphotons still carry recoverable correlation, and post-selection extracts contrast beyond what intensity imaging allows. The static configuration of Figure 3.2 isolates the role of S_2. With no scattering before the object, the strong source correlation is preserved at the object plane, so coincidence imaging already enhances contrast. We observed an MTF of 5.3 % against 3.05 % for the singles, approaching the two-fold enhancement expected of correlated illumination in the absence of scattering. Post-selection then nearly triples this again to reach 15.6 %, representing a five-fold enhancement over the singles and the largest relative improvement among the cases studied.

3.3 Correlation Imaging/Single Photon Scattering

In many quantum-imaging schemes, including ghost and correlation imaging, only one photon of each pair interacts with the object and the surrounding medium while its partner travels an undisturbed reference path. For a fixed scattering medium, this is often the preferable arrangement, since the correlation broadening is less severe when only one photon is scattered than when both traverse the same screens. To demonstrate the method in this geometry, a beam splitter placed in the far field of the crystal separates the signal and idler into an object arm and a reference arm immediately after generation. In the object arm, the photon passes through SLM1, the object at the crystal's image plane, and SLM2; the reference photon propagates directly to a separate region of the camera without encountering any scattering. Spatially resolved coincidences between the two arms are

recorded as before, and the same post-selection and window-summing procedure is applied. The object is the same three-line amplitude target used in the two-photon configuration, allowing a direct comparison between the two geometries.

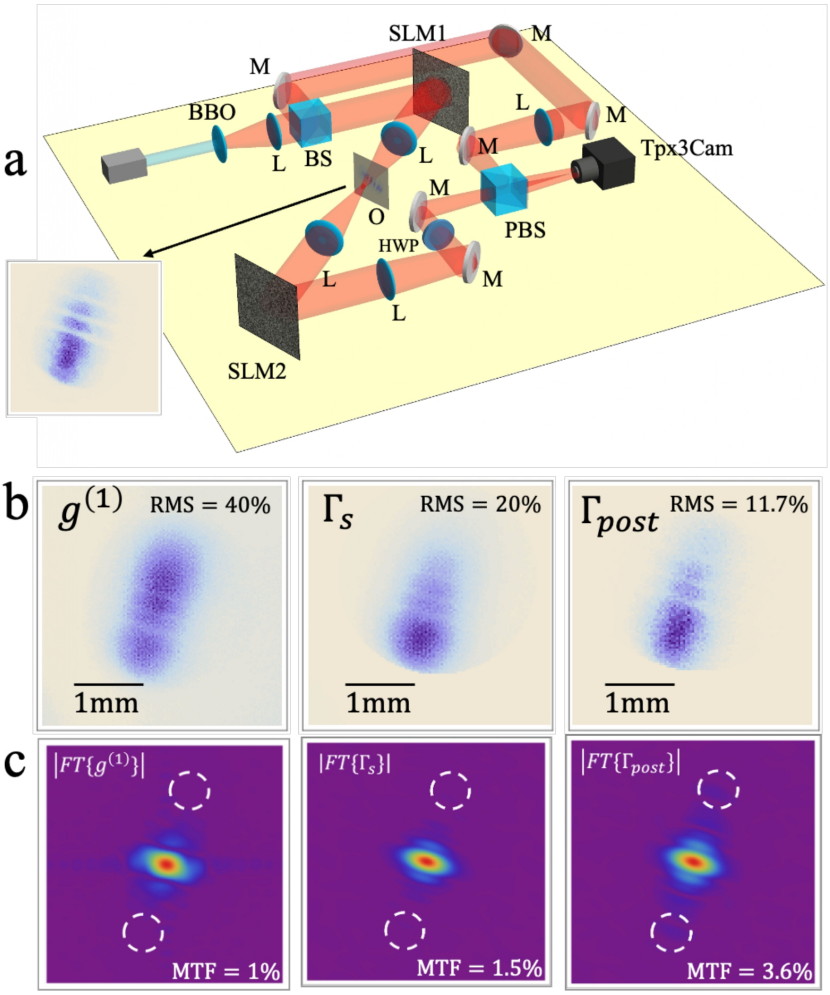


Figure 3.4. Correlation imaging with dynamic scattering media ($w_q/w_A \approx 6.8$). Random phase patterns act only in the object arm, displayed on SLM1 (before the object) and SLM2 (after the object) and varied over the acquisition, so the recorded coincidences average over several independent scattering realizations; the reference photon propagates unscattered. The singles image is degraded, and the non-post-selected coincidence image offers only moderate enhancement in this configuration; the post-selected image recovers the object, which confirms that correlation information can be recovered even when a single photon interacts with the object, so long as the reference photon preserves the correlation needed for post-selection. From the Fourier spectra, the MTF is estimated at 1% ($g^{(1)}$), 1.5% (Γ_s), and 3.6% ($\Gamma^{(3)}_{post}$).

Figure 3.4 reports a dynamic-scattering measurement at $w_q/w_A \approx 6.8$. As in the two-photon case, the singles image is degraded by scattering and the non-post-selected coincidence image offers only moderate improvement (from an estimated MTF of 1 % to 1.5 %), while the post-selected image $\Gamma^{(3)}_{post}$ recovers the object features. The Fourier spectra confirm that post-selection preserves the higher spatial frequencies lost in the other two reconstructions, with a 3.6-fold gain over the singles and a 2.4-fold gain over the coincidences. This establishes that correlation-based filtering remains effective when only one photon interacts with the object and the medium, provided the reference photon preserves the correlation information that post-selection relies on.

As an applied illustration of what this recovers, the same single-photon-scattering configuration was used to image an insect wing. Under sufficiently strong scattering, the fine venation becomes unrecognisable in the direct and coincidence images, and ordinary digital filtering does not restore it; the post-selected image, especially after a Laplacian-of-Gaussian filter, makes the veins visible again. This is a concrete demonstration that correlation post-selection recovers structural detail that scattering would otherwise scramble beyond recognition.

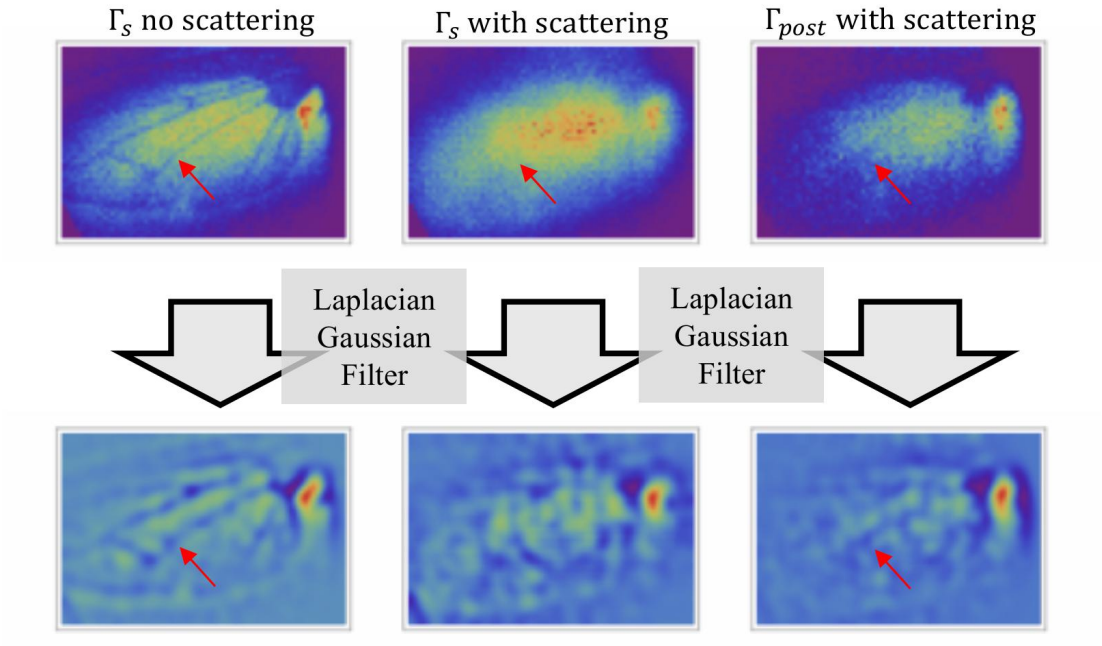


Figure 3.5. Retrieving image details by correlation post-selection (single-photon-scattering configuration). The object is an insect wing. Scattering renders the venation unrecognizable in both the direct and the coincidence images, and digital filtering does not restore it; the post-selected image recovers the veins, most clearly after a Laplacian-of-Gaussian filter is applied. The corresponding images in the absence of scattering, before and after filtering, are shown for comparison.

This is a concrete demonstration that correlation post-selection recovers structural detail that scattering would otherwise scramble beyond recognition. Figure 3.5 also clarifies a broader point: the enhancement is not tied to the periodic targets used to quantify it. The post-selection acts on the photon correlations, never on the image content, so nothing in the method favors a particular object — the line target simply reduces the contrast to a single MTF number, whereas the wing's venation was irregular and unknown in advance. Phase objects, however, remain untested and are left to future work.

3.4 Manuscript

The published manuscript is reproduced in full on the following pages.

Contrast enhanced imaging through weakly scattering media with spatially entangled photons

Alessio D'Errico,[1,2,*] James Hubble[†],[1,2] Rojan Abolhassani[†],[1,2] Nazanin Dehghan,[1,2] Yishai Klein,[1,2] Yingwen Zhang,[1,2] and Ebrahim Karimi[1,2,3]

[1]*Nexus for Quantum Technologies, University of Ottawa, Ottawa, K1N 6N5, ON, Canada*
[2]*National Research Council of Canada, 100 Sussex Drive, K1A 0R6, Ottawa, ON, Canada*
[3]*Institute for Quantum Studies, Chapman University, Orange, California 92866, USA*

Improving the image contrast of objects immersed in weakly scattering media can be achieved using various strategies. One common approach is to reject events associated with scattered photons in favor of the detection of ballistic photons. While this is traditionally done via time gating or spatial filtering, we propose a different approach based on probing the object with spatio-temporally entangled photon pairs. We show that coincidence detection, followed by post-selection on spatially correlated events, allows us to isolate ballistic from scattered bi-photons, thereby enhancing image contrast relative to a single-photon detection strategy, and simultaneously removes events due to background light. Our predictions are obtained via numerical simulations and confirmed by experiments conducted in two configurations where either both photons or only one illuminates the scene. In both scenarios, correlation post-selection shows an improvement in image contrast at the expense of higher shot noise due to the lower number of events. The latter can be partially compensated for by appropriately combining events from several post-selection windows. Our findings will enable extending imaging through scattering media into the quantum imaging framework in settings where adaptive optics, time gating, and spatial filtering are impractical.

arXiv:2605.28998v2 [quant-ph] 10 Jul 2026

I. INTRODUCTION

Imaging techniques, from microscopy and light detection and ranging to astronomy, can be affected by unknown inhomogeneities in the medium between the source and detector, resulting in a loss of image quality, quantified in terms of resolution and/or contrast [1, 2]. Whether the medium is a turbulent atmosphere, fog, a multi-mode waveguide, or tissue, the propagation of light is altered by phase aberrations, scattering, and coherence loss [2–4].

A common challenge in classical and quantum optical imaging is to devise techniques to address these undesired effects and recover image quality. A broad range of approaches has been proposed, which can be grouped into a few categories: filtering techniques [5–11], in which one aims to isolate the components of the light field that carry residual information about the object; numerical analysis [4, 11, 12], where knowledge of the physical properties of the scattering medium is used to recover effective point spread functions; and correction methods [13–17], where the scattering medium is experimentally characterized and its effect is compensated for using spatial light modulators.

The extension of these approaches to the few-photon regime is demanded by the growing potential of quantum imaging techniques, which use entangled two-photon states and spatially resolved coincidence detection [18–20]. Two photon correlations in different degrees of freedom of light have been investigated in various complex media, revealing migration of entanglement in specific sets of scattering modes [21–23], unique features in the correlation speckles [24–26], survival of polarization entanglement [27], and enhanced effects, for instance, in coherent back-scattering [28]. Moreover, spatio-temporal correlations can be employed to devise novel adaptive optics techniques directly applicable at the single photon level [29–34].

Hitherto, the introduction of filtering techniques in the quantum optical regime has been mostly limited to time-correlation-based methods [35], specifically in quantum LIDAR experiments [33]. In classical optics, filtering techniques try to distinguish and isolate different light paths through the medium. Generally speaking, one can distinguish between ballistic photons, which propagate undisturbed through the medium, and scattered photons, whose optical paths are modified one or more times by scattering centers (Figure 1-a). In [10], the authors also define "snake-photons" corresponding to photons whose optical path is only weakly modified with respect to the ballistic photons. Filtering methods are effective in weakly scattering regimes, where the thickness of the medium is at most of the same order as the mean scattering length, l_s, so that the ballistic photon contributions are still significant. When using pulsed light illumination, scattered photons can be filtered out using time-gating techniques [36–38], which exploit the fact that ballistic photons are the first to reach the detector. Under continuous-wave (cw) illumination, spatial or coherence filtering techniques can also be used [5]. Furthermore, these techniques can be combined with polarization filtering, where one makes use of the fact that scattered photons can accumulate a different polarization with respect to the input radiation [39].

In thin scattering media, scattering primarily manifests as transversely varying random phase shifts. In this regime, conventional rejection strategies are often ineffective or impractical: time gating requires ultrashort pulses or broadband light with very low coherence length, polarization filtering provides little benefit in the absence of significant anisotropy, and spatial filtering inevitably sacrifices resolution. At the same time, even a thin scattering layer can substantially reduce image contrast, making it necessary to develop alternative methods for discriminating ballistic light from scattered contributions.

Here, we address this problem using spatially entangled

[†] These authors contributed equally to this work.

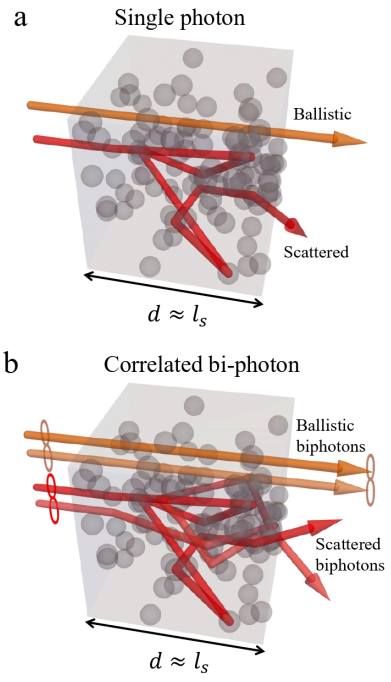


Figure 1. **Conceptual scheme**. **a,** In weakly scattering media (thickness d no longer than ~ 5 times the mean free path l_s) is possible to identify ballistic photons and isolate them from scattering events either using time gating or spatial filtering. Ballistic photons carry information on objects hidden behind or inside the scattering medium. **b,** In this work, we propose exploiting the fact that ballistic photon pairs preserve transverse position entanglement, and, thus, can be isolated from scattered biphotons via correlation post-selection.

photon pairs as the illumination source. As illustrated in Fig. 1-b, our approach exploits the fact that propagation through a scattering medium degrades the spatial correlations between entangled photon pairs. By contrast, photon pairs that follow ballistic or near-ballistic, "snake"-like paths can largely preserve their initial spatial correlations. We, therefore, suppress scattered biphoton contributions by postselecting coincidence events whose detected transverse coordinates remain consistent with the correlations before propagation through the medium. In this way, our method combines quantum spatial correlations with coincidence-based postselection to enhance the imaging contrast of objects embedded in weakly scattering media.

We first verify our predictions through numerical simulations, examining how the achievable contrast enhancement depends on the scattering strength and the degree of source entanglement. Then, we experimentally benchmark the method by demonstrating contrast enhancement under both dynamic and static scattering conditions, using two configurations: one in which both photons illuminate the object and propagate through the scattering medium, and another in which only one photon of the pair interacts with the object and undergoes scattering while the other acts as a reference.

II. SIMULATIONS

We consider the simplified problem of imaging an object O, characterized by a spatially variable transmission function $O(x)$, immersed in a weakly scattering medium consisting of random phase masks (S1 and S2) placed in the far field of O. The masks are placed both before and after the object, as illustrated in Figure 2-a. The choice to place S1 and S2 in planes conjugate to the object plane is motivated by the fact that these phase distortions will be the ones most severely affecting the imaging system. The system is probed by a pair of frequency-degenerate, spatially entangled photons (EPS). Indicating with q_i, q_s the transverse wave-vector components of idler and signal photons, the input state can be described by the bi-photon wavefunction

$$\psi(q_i, q_s) = \exp\left(-\frac{(q_i - q_s)^2}{w_q^2}\right) \exp\left(-\frac{(q_i + q_s)^2}{w_0^2}\right), \quad (1)$$

where we assumed a typical double-Gaussian approximation [20, 40], with w_q and w_0 respectively indicating the characteristic width of the phase-matching function and the pump amplitude in momentum space. For simplicity, we consider a 1D spatial coordinate, this treating the two-photon propagation as a 2D problem. This significantly reduces the computational time for the simulations.

In typical SPDC sources, $w_q \gg w_0$, which implies that photon pairs are strongly anti-correlated in transverse momentum and correlated in transverse position (considered in any plane where the source is imaged) [20, 40]. The correlation strength can thus be measured from the ratio w_q/w_0. The random phase masks act directly in the transverse momentum space – which, apart from a scaling factor, correspond to the far-field of the source – as follows:

$$\psi(q_i, q_s) \to e^{i(\varphi^{(r)}(q_i) + \varphi^{(r)}(q_s))} \psi(q_i, q_s), \quad (2)$$

where $\varphi^{(r)}(q)$ is a random phase, with the superscript $r = 1, \ldots, R$ indicating a specific realization selected from an ensemble of R elements. In both simulations and experiments, these phase screens were generated as lists of uniformly distributed random numbers in the interval $[-\pi, \pi]$. The number of elements in the list approximately fixed the scattering strength, while, prior to the simulations, the list was interpolated to extract an array with the same resolution as the chosen simulation window $M = 2^9$ pixels – see Supplementary Figure S2 for a detailed illustration.

To quantify the scattering strength, we first calculate the disorder-averaged autocorrelation function of the phase masks $A(x) = \frac{1}{R}\sum_r \sum_{x'} \varphi^{(r)}(x - x')\varphi^{(r)}(x')$. For a sufficiently large R, $A(x)$ is well approximated by a Gaussian of width w_A. This allows us to quantify the scattering strength by the ratio w_q/w_A: If $w_q < w_A$, the two photons, despite being spatially anti-correlated, will, on average, experience similar phase shifts and will still be strongly correlated in the near-field. Instead, for $w_q > w_A$ (see Fig. 2-b), each photon will acquire

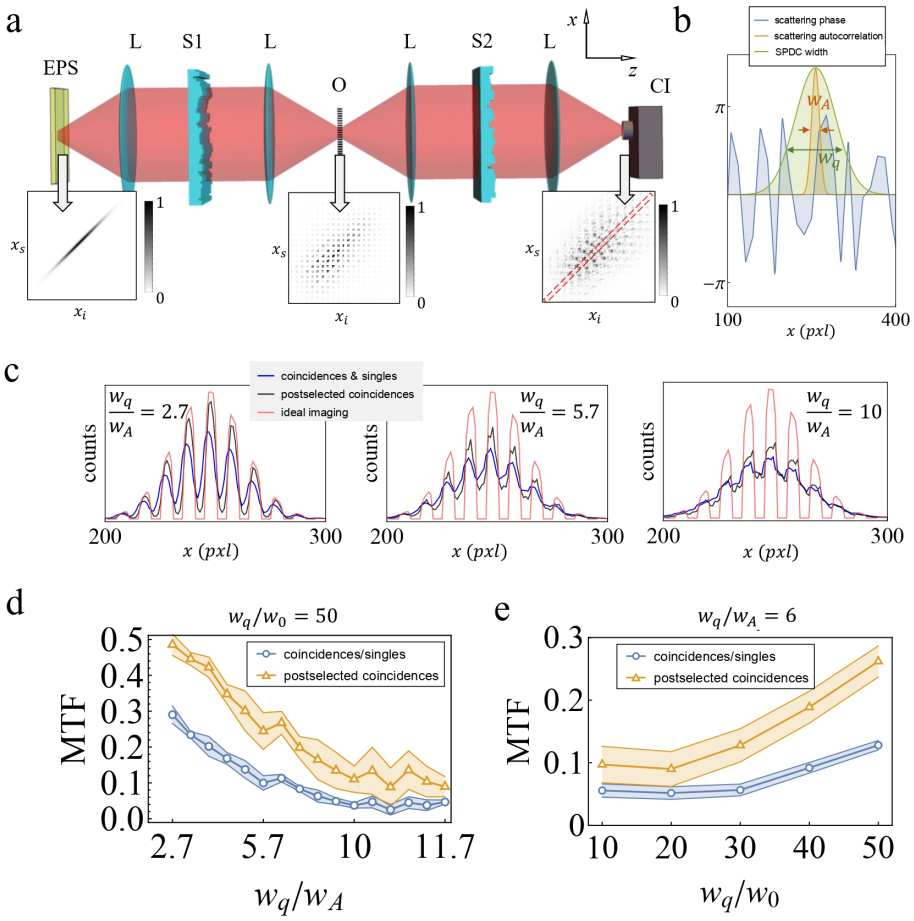


Figure 2. **Numerical simulations. a,** Scheme of the simulated setup: spatially entangled photon pairs (EPS) are propagated in free-space to a random phase screen (S1) placed in the far field of the source. Then the pair is incident on an object (O), with spatially varying transmissivity, placed in the source image plane. A second random phase screen (S2) is placed in the object's far field. Coincidence imaging (CI) is performed on the source/object image plane. L indicates lenses performing optical Fourier transforms. Insets show the spatial correlations (for a single scattering realization) along the x-coordinate in different propagation planes. The red dashed rectangle indicates the numerically post-selected region in the correlation space. **b,** Plots illustrating the definitions and relative size comparison of characteristic widths of the problem. The far-field anti-correlation width w_q is compared with the autocorrelation width w_A that characterizes the scattering strength of the phase masks considered (the blue line shows a single realization of the scattering). **c,** Reconstructed images of the object for different relative scattering strengths obtained after averaging the spatial correlations over 100 scattering realizations. Red curves indicate the ground truth that would be observed in the absence of scattering. Blue curves are obtained by summing the correlation plots along the x_i coordinate; this curve is the same for the cases of using singles or total coincidence counts. Black curves instead are obtained from spatial correlation post selection, as shown by the diagonal region outlined by the red dashed line in panel **a**. **d,** Image contrast (measured by the MTF in Eq. (3)) as a function of the relative scattering strength w_q/w_A for fixed input correlation strength $w_q/w_0 = 50$. The contrast is higher for post-selected coincidences at all considered strengths, although the advantage reduces for strong scattering, where ballistic biphotons become scarce. Panel **e** shows that, for a fixed relative scattering strength, the contrast enhancement grows monotonically with the strength of the spatial correlations of the input state. Results in d and e are averaged over multiple simulation runs. Each run considered 100 scattering realizations. Colored bands show the standard deviations over all runs. All counts are normalized and reported in arbitrary units.

a randomly different phase factor. The Fourier transform of the resulting bi-photon wavefunction (corresponding to the state in the object plane) will be largely uncorrelated (see, e.g. inset in Fig. 2-a in correspondence of O). We note that the ratio w_q/w_A is a convenient definition of the scattering strength since it can be directly estimated from correlation measurements (see Supplementary S1 and Supplementary Figure S5).

The detrimental role of the scattering before and after the

object can be understood as follows: 1) The random mask S1 between source and object scrambles the two-photon correlations, hence affecting the advantage offered by sub-shot noise quantum imaging; 2) the mask S2 between object and detector reduces the image contrast also when incoherent illumination is employed. For incoherent light, only S2 affects image quality, whereas for coincidence imaging of correlated photons, both S1 and S2 have undesired effects. Specifically, one could expect that, with S1 in place, we would lose any advantage in using spatially correlated photons. As we explain below, our numerical simulations show that this is not the case, and that the analysis of coincidence images of spatially entangled photons can yield contrast enhancement beyond what is allowed by standard intensity imaging.

The crucial idea is to collect coincidences $\Gamma(x_i, x_s) \propto |\psi(x_i, x_s)|^2$ in the source/object image plane and select those events for which $x_i \approx x_s$. A *coincidence image* is typically obtained by observing the marginal with respect to the position of the idler photon $\Gamma_s(x_s) = \sum_{x_i} \Gamma(x_i, x_s)$ (corresponding to the blue lines in Fig. 2-c). In the presence of scattering, the image contrast in Γ_s will be strongly reduced. In this case, most scattered photon pairs will populate events outside the diagonal of the correlation matrix, while ballistic biphotons will contribute to events along the diagonal. We thus expect that the *postselected image* $\Gamma_{post} := \Gamma(x_i = x_s)$ contains a higher relative number of ballistic contributions compared to $\Gamma_s(x)$ and should thereby exhibit higher contrast.

Figure 2-c shows some examples of this contrast enhancement where we simulate, for different scattering strengths, the imaging of an object consisting of a regular array of apertures. In all these cases, the postselected coincidences $\Gamma_{post}(x)$ exhibit a higher contrast with respect to the coincidence image $\Gamma_s(x)$ (which, in the context of these simulations, is also formally equivalent to the expected result of intensity measurements). All the results shown are obtained from coincidences averaged over multiple scattering realizations ($R = 100$), which corresponds to experimentally imaging objects immersed in dynamic scattering media – the static case is illustrated in Supplementary figure S1.

To estimate the contrast enhancement more quantitatively, we measure the resulting contrast through a Modulation Transfer Function (MTF) defined as follows. Let $I_{scatt}(x)$ be the coincidence image with the scattering medium and $I_{true}(x)$ the ground truth, i.e. the image with no scattering. The object chosen for the simulations is such that the Fourier transform of $I_{true}(x)$ has one dominant non-zero spatial frequency k_0. $I_{scatt}(x)$ will have lower frequency contributions due to the reduced image contrast. We define the MTF as the ratio between the nonzero and the zero frequency contributions:

$$\text{MTF} = \frac{\max\{|FT[I_{scatt}](k \approx k_0)|\}}{\max\{|FT[I_{scatt}](k \approx 0)|\}}, \tag{3}$$

with FT indicating the Fourier transform. We thus evaluate the MTF for different scattering strengths (with a fixed correlation strength). Figure 2-d shows the MTF averaged over multiple runs (with the standard deviation given by the colored bands). It is evident that the post-selection correlation yields contrast enhancement for $w_q/w_A \lesssim 10$. For stronger scattering, the enhancement decreases due to the reduced number of ballistic bi-photons. In Fig. 2-e, we confirm that the contrast enhancement is allowed by the entanglement of the input two-photon state: stronger correlations (proportional to w_q/w_0) yield higher MTF enhancement when fixing the scattering strength. Note that, while we kept the ratio w_q/w_0 between 10 and 50 to avoid the necessity of high-resolution simulations, experimentally it is easy to reach ratios $w_q/w_0 > 100$ [41, 42].

The simulations have been carried out considering only one transverse coordinate to bypass the computational difficulty of propagating the biphoton wavefunction dependent on the 4-spatial coordinates of idler and signal photons. We address the general case of two-dimensional objects and scattering phase-masks in the following experimental section.

III. EXPERIMENTAL RESULTS

A. Two photon scattering

To verify the contrast enhancement allowed by coincidence postselection, we performed a couple of proof-of-principle experiments using spatially correlated photon pairs generated via spontaneous parametric down-conversion (SPDC) in a 1 mm-thick Type-I β-barium borate (BBO) crystal pumped by a pulsed 405 nm laser. In the experiment, frequency-degenerate photons at 810 nm were spectrally filtered using bandpass filters with 10 nm bandwidth. Reflective liquid-crystal spatial light modulators (LC-SLMs) were used to introduce random phase patterns onto the down-converted beams. A conceptual scheme of the experiment is sketched in Fig. 3-a, which was designed to reproduce the conditions considered in the numerical simulations (Fig. 2-a). The object O consisted of 3 dark lines drawn with a black marker on a transparent plastic fragment (see Supplementary Information). The inset in Fig. 3-a shows the appearance of the object on the camera plane in the absence of scattering. In this first configuration, the photon pairs travel along the same beam path but are spatially anti-correlated in the far field, where each photon interacts with a different region of the scattering screens SLM1 and SLM2. The relay imaging system re-images the crystal plane onto the object location, where the photon pairs overlap. In order to spatially resolve two photo coincidences, signal and idler photons were probabilistically separated in two different optical paths and detected on corresponding regions of a time-stamping camera (Tpx3Cam) equipped with an image intensifier for single-photon detection [43]. The Tpx3Cam records the arrival time and the spatial coordinates of each event with $\sim$ 7 ns resolution [44]. From these data, we can extract a list of coincidences between two separate regions of interest (ROIs) on the camera sensor. Here, a coincidence event is defined by two photons arriving within 10 ns of each other.

The resulting data set consists of a compressed format of the four-dimensional coincidence distribution $\Gamma(\mathbf{x}_i, \mathbf{x}_s)$, which records all spatial correlations between photon pairs. An example of spatial correlations in the near field after scattering is shown in Fig. 3-b. The presence of scattering media broadens the spatial correlations along both the x and y coordinates,

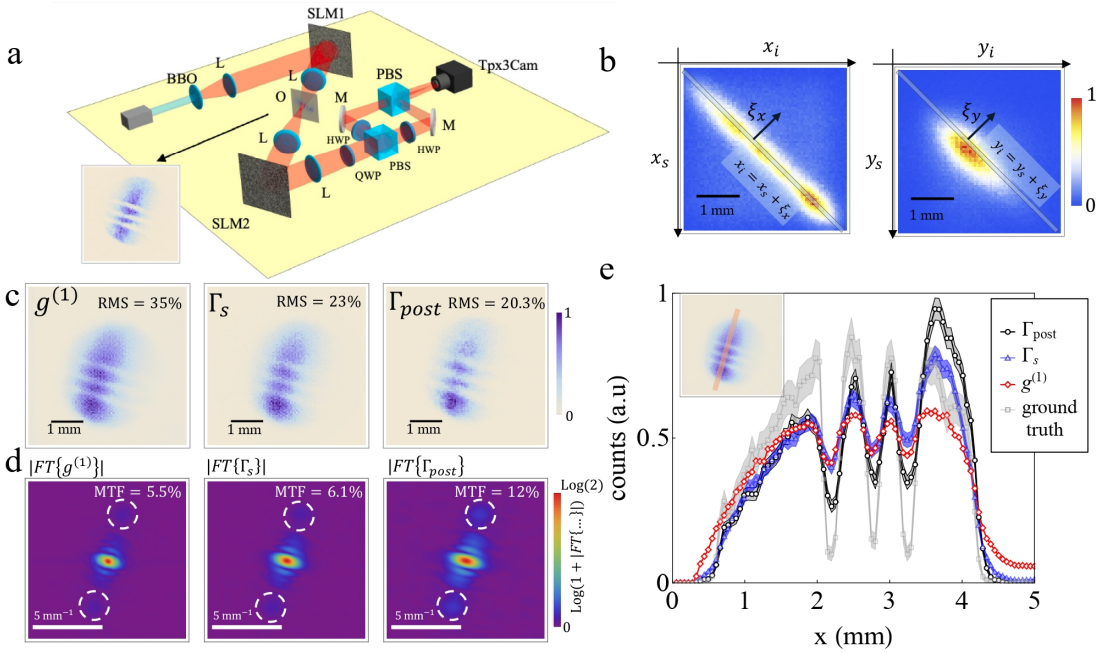


Figure 3. **Experimental setup and results. a,** Outline of the experimental setup. BBO, β-barium borate crystal cut for Type I SPDC. SLM1 and SLM2 are liquid crystal spatial light modulators used to introduce scattering in S1 and S2 planes, respectively. O is the amplitude sample to be imaged. L, Lens; M, mirror; BS, beam splitter. Spatially resolved coincidences are collected by a time-stamping camera, Tpx3Cam. **b,** Near field correlations after scattering. Coincidence postselection is obtained by selecting events where signal and idler coordinates are linearly correlated $\mathbf{x}_i = \mathbf{x}_s + \boldsymbol{\xi}$. **c,** Image of the object immersed in a dynamic scattering medium as reconstructed by singles ($g^{(1)}$), coincidences (Γ_s), and post-selected coincidences (Γ_{post}). Γ_{post} is obtained by summing 6×6 postselection images –i.e. 36 different choices of $\boldsymbol{\xi}$– to reduce shot noise (see text for details). Γ_{post} demonstrates an enhanced contrast, as highlighted in **d** and **e**. RMS indicates the root-mean-square error when comparing each output with the ground truth (for which we used the inset of panel **a**). **d**, 2D Fourier spatial spectra of the images in **b**. The contrast enhancement corresponds to the increased relative brightness of the spatial frequencies evidenced by the dashed white circles. All 2D plots are normalized with respect to the maximum. From the results in **d**, we estimated the MTF to be $5.5\,\%, 6.1\,\%$, and $12\,\%$, respectively. **e,** 1D cross-section of each image (indicated by the dashed red line in the inset) with error bands corresponding to 3 times the standard error. The scattering strength for the data shown in this figure was estimated to be approximately $w_q/w_A \approx 3.4$.

which, in the absence of scattering, are only ~ 1.5 pixel wide.

To isolate ballistic photons from the scattered background, we select events where idler and signal positions differ by a fixed amount: $\mathbf{x}_i = \mathbf{x}_s + \boldsymbol{\xi}$, as illustrated by the rectangular shades in Fig. 3-b. The resulting postselected images $\Gamma_{\text{post}}(\mathbf{x}; \boldsymbol{\xi}) := \Gamma(\mathbf{x}_i = \mathbf{x}_s + \boldsymbol{\xi})$ are expected to yield contrast enhancement. This spatial filtering preferentially retains ballistic photons that maintain their correlation, while rejecting scattered photons that no longer exhibit spatial correlation. At the same time, due to the lower number of associated events, Γ_{post} will also exhibit higher shot noise. More events can be included by choosing different offsets $\boldsymbol{\xi}$, which give only a rigid translation of the corresponding postselected image.

The final images are obtained by summing $n \times n$ postselected images after each image has been appropriately shifted: $\Gamma^{(n)}_{\text{post}}(\mathbf{x}) = \sum_{\xi_x,\xi_y=1,\dots,n} \Gamma_{\text{post}}(\mathbf{x} - \boldsymbol{\xi}, \boldsymbol{\xi})$. For all the experimental acquisitions, we recorded 500 frames at 20 s per frame.

Figure 3-c shows a comparison between classical single-photon imaging ($g^{(1)}$), non-post-selected coincidence imaging (Γ_s), and post-selected coincidence imaging (Γ^n_{post}, with $n = 6$) for a test object immersed in dynamic scattering media. The scattering strength for this measurement was estimated to be approximately $w_q/w_A \approx 5.7$. The estimate was made by measuring the ratio of the measured correlation widths with and without scattering. The non-post-selected coincidence image Γ_s shows only marginal improvement when compared with the direct image $g^{(1)}$. In contrast, the post-selected coincidence image $\Gamma^{(n=6)}_{\text{post}}$ reveals the object features with dramatically enhanced contrast. Results for other values of n are shown in the supplementary. Each image was compared with the ground truth (inset in panel a), by evaluating the root-mean-square difference RMS $:= \sum_i |I^g_i - I^r_i| / \sum_h (I^g_h + I^r_h)$ with I^g being the ground truth image and $I^r = g^{(1)}, \Gamma_s, \Gamma_{post}$. Coincidence images show an improvement in the RMS with respect to the ground truth; however, the relative improvement for Γ_{post} with respect to Γ_s is marginal due to the increased noise in the postselected image. The advantage of the postselection is more evident when targeting a measure of the contrast, which

is more robust to noise fluctuations.

The contrast enhancement is quantified through the modulation transfer function (MTF), calculated from the 2D Fourier spatial spectra shown in Fig. 3-d. All 2D plots are normalized with respect to their respective maxima. From the results in Fig. 3-d, we estimated the MTF to be 5.5% for the singles ($g^{(1)}$), 6.1% for non-post-selected coincidences (Γ_s), and 12% for post-selected coincidences (Γ_{post}). The MTF was obtained from the ratio between the maximum values within the regions highlighted by the dashed circles and the central (zero-frequency) maximum. Post-selection provides more than a two-fold improvement in MTF over the direct imaging and nearly doubles the MTF compared to non-post-selected coincidences.

The contrast enhancement is further illustrated in the 1D cross-sections shown in Fig. 3-e. While the singles profile and the non-post-selected coincidence profile show only faint object features, the post-selected profile exhibits significantly enhanced contrast. The error bands, corresponding to three times the standard error, confirm that the observed differences between profiles are well above the measurement uncertainty. This demonstrates that spatial correlations in biphoton states can effectively filter ballistic photons from scattered background, even in the presence of dynamic scattering. Moreover, the fact that the error band in $\Gamma_{pos}^{(n=6)}$ is of the same order than for the other two datasets shows how summing over multiple postselected images helps reducing the shot noise by retaining the contrast enhancement.

B. Single photon scattering

Until now, we have considered the configuration in which both photons propagate through the scattering medium. In several quantum imaging experiments, including ghost imaging and correlation imaging, only one of the two photons passes through the object and surrounding scattering media. This may often be a preferred scenario, since, for a fixed scattering medium, the spatial correlation broadening is expected to be less severe when only one photon is affected than when both photons traverse the same scattering screens. To demonstrate this approach, we implemented a correlation imaging configuration where signal and idler photons are separated immediately after generation (Fig. 4a). A beam splitter positioned in the far field of the crystal directs photons into an object arm and a reference arm. In the object arm, the signal photon traverses through scattering screen SLM1, the object positioned at the crystal's image plane, and scattering screen SLM2. The reference arm photon propagates directly to a separate region of the camera sensor without encountering any scattering. Spatially resolved coincidences between the two arms are then recorded with a time-stamping camera (Tpx3Cam). The data acquisition and analysis procedures follow those described for Fig. 3, with 500 frames at 20 s per frame. Figure 4b shows the comparison between singles ($g^{(1)}$), non-post-selected coincidences (Γ_s), and post-selected coincidences ($\Gamma_{\text{post}}^{(n=3)}$) for an object imaging through dynamic scattering in the object arm. The singles' image shows degradation due to scattering. The non-post-selected coincidence image (Γ_s) shows only marginal improvement. Instead, the post-selected image ($\Gamma_{\text{post}}^{(n=3)}$ reveals enhanced contrast, demonstrating that the post-selection can recover correlation information even when only one photon interacts with the object.

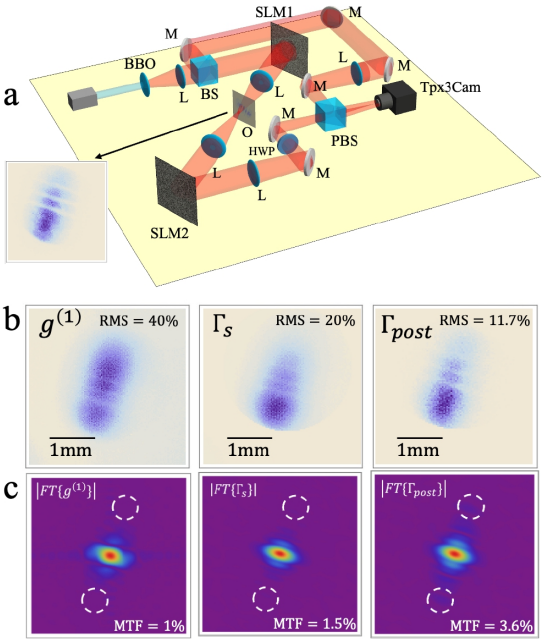


Figure 4. **Correlation imaging with dynamic scattering. a,** Outline of the experimental setup for correlation imaging. BBO, β-barium borate crystal cut for Type I SPDC. A beam splitter (BS) in the far field separates signal and idler photons into an object arm and a reference arm. SLM1 and SLM2 are liquid crystal spatial light modulators used to introduce scattering. O is the amplitude sample to be imaged. L, Lens; M, mirror; BS, beam splitter. Spatially resolved coincidences are collected by a time-stamping camera, Tpx3Cam. **b,** Image of the object immersed in a dynamic scattering medium as reconstructed by singles ($g^{(1)}$), coincidences (Γ_s), and post-selected coincidences ($\Gamma_{\text{post}}^{(n=3)}$). RMS values are, respectively, 40%, 20%, 11.7%. **c,** 2D Fourier spatial spectra of the images in **b**. The contrast enhancement corresponds to the increased relative brightness of the spatial frequencies encircled by the dashed white circles. From the results in **c**, we estimated the MTF to be 1 %, 1.5 %, 3.6 %, respectively. The scattering strength for the data shown in the figure was estimated to be approximately $w_q/w_A \approx 6.8$.

The contrast enhancement is again evident when analyzing the MTF. The 2D Fourier spatial spectra in Fig. 4c, demonstrate the preservation of higher spatial frequencies in the post-selected image (indicated by the dashed white circles). From the Fourier spectra, we estimated the MTF to be 4.52% for singles ($g^{(1)}$), 3.55% for non-post-selected coincidences (Γ_s), and 6.92% for post-selected coincidences ($\Gamma_{\text{post}}^{(n=3)}$). Post-selection provides approximately 50% improvement over singles and nearly doubles the MTF compared to non-post-selected coin-

cidences. This demonstrates that correlation-based filtering remains effective even when only one photon interacts with the object and scattering medium, while the reference photon preserves the spatial correlation information needed for post-selection.

As an applied example, we illustrate how the postselected images can allow for identifying features otherwise not recognizable by direct or coincidence imaging. In the example reported in Fig. 5, the object consisted of an insect wing. Under the effect of sufficiently strong scattering– here applied on one of the two photons–fine details, like veins, become completely unrecognizable, even when processing the image with digital filters. As shown in Fig. 5, postselection images can instead help to identify these details, as is more evident when a Laplacian-Gaussian filter is applied.

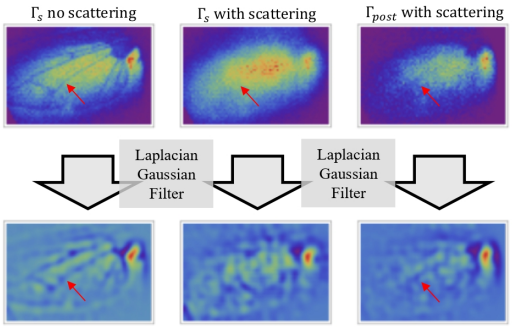


Figure 5. **Retrieving image details from correlation postselection.** Postselection of correlation data allows to recover object details that would otherwise be completely scrambled by the scattering medium. In this example, where the object is an insect wing, it is seen how scattering hides the venation pattern. Some of the veins are, however, slightly visible when looking at the postselection data. This is more evident when digital filtering is applied to the recovered images. The corresponding images in the absence of scattering (before and after digital filtering) are shown on the left for comparison. These data were acquired in the single-photon-scattering configuration.

IV. CONCLUSION

We have demonstrated that spatial post-selection of correlated photon pairs enables contrast-enhanced imaging through dynamic and static scattering media. Our experimental results show that post-selection can recover object features that are generally obscured by scattering, with modulation transfer function improvements of up to two-fold over non-post-selected coincidences and several-fold over classical single-photon imaging. This enhancement persists across different experimental configurations, including biphoton imaging, where both photons traverse scattering screens and correlation imaging, where only one photon interacts with the object.

The key mechanism underlying this enhancement is the spatial filtering of ballistic photons through coincidence post-selection. By selecting photon pairs that maintain specific spatial correlations $\mathbf{x}_i = \mathbf{x}_s + \boldsymbol{\xi}$, we preferentially retain photons that have not been significantly scattered, while rejecting those that have lost their correlation due to random phase shifts.

Future work could explore several promising directions for improvement and extension. While here we focused on the detection of amplitude objects, possible generalizations to phase objects [45–48] remain to be tested.

The approach introduced in this work could offer advantages over other classical techniques in experiments involving thin scattering media, where scattered photons experience strong phase distortions but small – below ps – temporal delays, making time gating difficult. Moreover, this technique is directly applicable in applications requiring low illumination to avoid photo-damage. Further suppression of scattered photons could be achieved by combining this technique with temporal gating employing the pump laser for a nonlinear optical switch [36, 38].

Furthermore, integrating adaptive optics strategies could be employed to mitigate higher levels of scattering [32, 49–51], hypothetically enabling imaging through even more strongly scattering media.

V. ACKNOWLEDGMENTS

This work was supported by the Canada Research Chair (CRC) Program, NRC-uOttawa Joint Centre for Extreme Quantum Photonics (JCEP) via the Quantum Sensors Challenge Program at the National Research Council of Canada, and Quantum Enhanced Sensing and Imaging (QuEnSI) Alliance Consortia Quantum grant.

[1] Stefan Rotter and Sylvain Gigan, "Light fields in complex media: Mesoscopic scattering meets wave control," Reviews of Modern Physics **89**, 015005 (2017).
[2] Jacopo Bertolotti and Ori Katz, "Imaging in complex media," Nature Physics **18**, 1008–1017 (2022).
[3] Eric Akkermans and Gilles Montambaux, *Mesoscopic physics of electrons and photons* (Cambridge university press, 2007).
[4] Seokchan Yoon, Moonseok Kim, Mooseok Jang, Youngwoon Choi, Wonjun Choi, Sungsam Kang, and Wonshik Choi, "Deep optical imaging within complex scattering media," Nature Reviews Physics **2**, 141–158 (2020).
[5] David Huang, Eric A Swanson, Charles P Lin, Joel S Schuman, William G Stinson, Warren Chang, Michael R Hee, Thomas Flotte, Kenton Gregory, Carmen A Puliafito, *et al.*, "Optical coherence tomography," science **254**, 1178–1181 (1991).

[6] Steven P Schilders, Xiaosong S Gan, and Min Gu, "Microscopic imaging through a turbid medium by use of annular objectives for angle gating," Applied optics **37**, 5320–5326 (1998).

[7] C Dunsby and PMW French, "Techniques for depth-resolved imaging through turbid media including coherence-gated imaging," Journal of Physics D: Applied Physics **36**, R207–R227 (2003).

[8] James Pawley, *Handbook of biological confocal microscopy*, Vol. 236 (Springer Science & Business Media, 2006).

[9] Warren R Zipfel, Rebecca M Williams, and Watt W Webb, "Nonlinear magic: multiphoton microscopy in the biosciences," Nature biotechnology **21**, 1369–1377 (2003).

[10] Min Gu and XS Gan, "Monte carlo simulation for confocal imaging through highly scattering media," Scanning **19**, 148–149 (1997).

[11] Min Gu, Xiaosong Gan, and Xiaoyuan Deng, "Microscopic imaging through turbid media," Springeer **5**, 201 (2015).

[12] Daniele Faccio, Andreas Velten, and Gordon Wetzstein, "Non-line-of-sight imaging," Nature Reviews Physics **2**, 318–327 (2020).

[13] Emmett N Leith and Juris Upatnieks, "Holographic imagery through diffusing media," Journal of the Optical Society of America **56**, 523–523 (1966).

[14] Sébastien M Popoff, Geoffroy Lerosey, Rémi Carminati, Mathias Fink, Albert Claude Boccara, and Sylvain Gigan, "Measuring the transmission matrix in optics: An approach to the study and control of light propagation in disordered media," Physical review letters **104**, 100601 (2010).

[15] Mickael Mounaix, Hugo Defienne, and Sylvain Gigan, "Deterministic light focusing in space and time through multiple scattering media with a time-resolved transmission matrix approach," Physical Review A **94**, 041802 (2016).

[16] Roarke Horstmeyer, Haowen Ruan, and Changhuei Yang, "Guidestar-assisted wavefront-shaping methods for focusing light into biological tissue," Nature photonics **9**, 563–571 (2015).

[17] Hui Cao, Allard Pieter Mosk, and Stefan Rotter, "Shaping the propagation of light in complex media," Nature Physics **18**, 994–1007 (2022).

[18] Paul-Antoine Moreau, Ermes Toninelli, Thomas Gregory, and Miles J Padgett, "Imaging with quantum states of light," Nature Reviews Physics **1**, 367–380 (2019).

[19] Hugo Defienne, Warwick P Bowen, Maria Chekhova, Gabriela Barreto Lemos, Dan Oron, Sven Ramelow, Nicolas Treps, and Daniele Faccio, "Advances in quantum imaging," Nature Photonics **18**, 1024–1036 (2024).

[20] Alessio D'Errico and Ebrahim Karimi, "Imaging of biphoton states: Fundamentals and applications," Advanced Functional Materials (2025), 10.1002/adfm.202526562.

[21] Ohad Lib and Yaron Bromberg, "Quantum light in complex media and its applications," Nature Physics **18**, 986–993 (2022).

[22] Natalia Herrera Valencia, Suraj Goel, Will McCutcheon, Hugo Defienne, and Mehul Malik, "Unscrambling entanglement through a complex medium," Nature Physics **16**, 1112–1116 (2020).

[23] Baptiste Courme, Chloé Vernière, Peter Svihra, Sylvain Gigan, Andrei Nomerotski, and Hugo Defienne, "Quantifying high-dimensional spatial entanglement with a single-photon-sensitive time-stamping camera," Optics letters **48**, 3439–3442 (2023).

[24] CWJ Beenakker, JWF Venderbos, and MP Van Exter, "Two-photon speckle as a probe of multi-dimensional entanglement," Physical review letters **102**, 193601 (2009).

[25] H Di Lorenzo Pires, J Woudenberg, and MP Van Exter, "Statistical properties of two-photon speckles," Physical Review A—Atomic, Molecular, and Optical Physics **85**, 033807 (2012).

[26] Avraham Klein, Oded Agam, and Boris Spivak, "Speckle statistics of entangled photons," Physical Review A **94**, 013828 (2016).

[27] Lingyan Shi, Enrique J Galvez, and Robert R Alfano, "Photon entanglement through brain tissue," Scientific reports **6**, 37714 (2016).

[28] Mamoon Safadi, Ohad Lib, Ho-Chun Lin, Chia Wei Hsu, Arthur Goetschy, and Yaron Bromberg, "Coherent backscattering of entangled photon pairs," Nature Physics **19**, 562–568 (2023).

[29] H Defienne, M Barbieri, Benoît Chalopin, Béatrice Chatel, IA Walmsley, BJ Smith, and S Gigan, "Nonclassical light manipulation in a multiple-scattering medium," Optics letters **39**, 6090–6093 (2014).

[30] Hugo Defienne, Matthew Reichert, and Jason W Fleischer, "Adaptive quantum optics with spatially entangled photon pairs," Physical review letters **121**, 233601 (2018).

[31] Ronen Shekel, Ohad Lib, Alon Sardas, and Yaron Bromberg, "Shaping entangled photons through emulated turbulent atmosphere," OSA Continuum **4**, 2339–2350 (2021).

[32] Patrick Cameron, Baptiste Courme, Chloé Vernière, Raj Pandya, Daniele Faccio, and Hugo Defienne, "Adaptive optical imaging with entangled photons," Science **383**, 1142–1148 (2024).

[33] Aongus McCarthy, Robert J Collins, Nils J Krichel, Verónica Fernández, Andrew M Wallace, and Gerald S Buller, "Long-range time-of-flight scanning sensor based on high-speed time-correlated single-photon counting," Applied optics **48**, 6241–6251 (2009).

[34] Kiran Bajar, Rounak Chatterjee, Vikas S Bhat, and Sushil Mujumdar, "Partial immunity of two-photon correlation against wavefront distortion for spatially entangled photons," APL Quantum **2** (2025).

[35] Zhe-Yu Jeff Ou, *Multi-photon quantum interference*, Vol. 43 (Springer, 2007).

[36] MA Duguay and J-W_ Hansen, "An ultrafast light gate," Applied physics letters **15**, 192–194 (1969).

[37] Michael R Hee, Joseph A Izatt, Joseph M Jacobson, James G Fujimoto, and Eric A Swanson, "Femtosecond transillumination optical coherence tomography," Optics letters **18**, 950–952 (1993).

[38] Yang Xu, Saumya Choudhary, Long D Nguyen, Matthew Klein, Shivashankar Vangala, J Keith Miller, Eric G Johnson, Joshua R Hendrickson, M Zahirul Alam, and Robert W Boyd, "Epsilon-near-zero time-gate for high-fidelity spatial information transfer through dynamic scattering media," Nature Communications (2026).

[39] X Gan, SP Schilders, and Min Gu, "Image enhancement through turbid media under a microscope by use of polarization gating methods," Journal of the Optical Society of America A **16**, 2177–2184 (1999).

[40] S. P. Walborn, C. H. Monken, S. Pádua, and P. H. Souto Ribeiro, "Spatial correlations in parametric down-conversion," Physics Reports **495**, 87–139 (2010).

[41] Fabrice Devaux, Alexis Mosset, Paul-Antoine Moreau, and Eric Lantz, "Imaging spatiotemporal hong-ou-mandel interference of biphoton states of extremely high schmidt number," Physical Review X **10**, 031031 (2020).

[42] Xiaoqin Gao, Yingwen Zhang, Alessio D'Errico, Khabat Heshami, and Ebrahim Karimi, "High-speed imaging of spatiotemporal correlations in hong-ou-mandel interference," Optics Express **30**, 19456–19464 (2022).

[43] Andrei Nomerotski, Matthew Chekhlov, Denis Dolzhenko, Rene Glazenborg, Brianna Farella, Michael Keach, Ryan Mahon, Dmitry Orlov, and Peter Svihra, "Intensified tpx3cam, a fast data-driven optical camera with nanosecond timing resolution

for single photon detection in quantum applications," Journal of Instrumentation **18**, C01023 (2023).
[44] Victor Vidyapin, Yingwen Zhang, Duncan England, and Benjamin Sussman, "Characterisation of a single photon event camera for quantum imaging," Scientific Reports **13**, 1009 (2023).
[45] Danilo Zia, Nazanin Dehghan, Alessio D'Errico, Fabio Sciarrino, and Ebrahim Karimi, "Interferometric imaging of amplitude and phase of spatial biphoton states," Nature Photonics **17**, 1009–1016 (2023).
[46] Giuseppe Ortolano, Alberto Paniate, Pauline Boucher, Carmine Napoli, Sarika Soman, Silvania F Pereira, Ivano Ruo-Berchera, and Marco Genovese, "Quantum enhanced non-interferometric quantitative phase imaging," Light: Science & Applications **12**, 171 (2023).
[47] Nazanin Dehghan, Alessio D'Errico, Francesco Di Colandrea, and Ebrahim Karimi, "Biphoton state reconstruction via phase retrieval methods," Optica **11**, 1115–1123 (2024).
[48] Nazanin Dehghan, Alessio D'Errico, Yingwen Zhang, Benjamin Sussman, and Ebrahim Karimi, "Diffraction of correlated biphotons through transparent samples," arXiv preprint arXiv:2410.22635 (2024).
[49] Lukas Scarfe, Felix Hufnagel, Manuel F Ferrer-Garcia, Alessio D'Errico, Khabat Heshami, and Ebrahim Karimi, "Fast adaptive optics for high-dimensional quantum communications in turbulent channels," Communications Physics **8**, 79 (2025).
[50] Chloé Vernière, Raphaël Guitter, Baptiste Courme, and Hugo Defienne, "Entanglement-enabled image transmission through complex media," Nature Physics , 1–8 (2026).
[51] Baptiste Courme, Chloé Vernière, Malo Joly, Daniele Faccio, Sylvain Gigan, and Hugo Defienne, "Non-classical optimization of entangled photons through complex media," Optica **13**, 968–976 (2026).

Author ContributionsAD and YK conceived the idea. AD developed the simulations. JH, RA, ND, and AD, with contributions from YK and YZ, built the experimental setup and collected the data. YZ, with contributions from AD, prepared the software for the extraction of post-selected correlation images. AD, YK, JH, and RA analyzed the results. AD, JH, and RA prepared the first version of the manuscript. EK supervised the project.

Data availability The data that support the findings of this study are available from the corresponding author upon reasonable request.

Code availability The code used for the data analysis is available from the corresponding author upon reasonable request.

Ethics declarations Competing Interests. The authors declare no competing interests.

Corresponding authors Correspondence and requests for materials should be addressed to the corresponding author.

Supplementary Material for: Contrast enhanced imaging through weakly scattering media with spatially entangled photons.

S1. GENERATION AND CHARACTERIZATION OF SCATTERING STRENGTH

The measured spatial correlations can be used to estimate the scattering strength w_q/w_A. In the case of the biphoton imaging, we find that a good estimate can be obtained from the relation (derived semiempirically from numerical simulations –see figure S4–)

$$w_-/w_{-,0} = \sqrt{1+3(w_q/w_A)^2} \tag{S1}$$

where $w_{-,0} = 2/w_q$ is the correlation width without scattering, and w_- the correlation width with scattering. In the case of correlation imaging the equation must be corrected as

$$w_-/w_{-,0} = \sqrt{(1+3(w_q/w_A)^2)/2}. \tag{S2}$$

The obtained results are in qualitative agreement with a direct measurement where the phase-matching intensity on the SLM plane was measured and directly compared with the applied holograms. However, the phase-matching function exhibits a longitudinal walk-off for which the Gaussian approximation is only a rough estimate.

S2. RESULT FOR DIFFERENT N SCANS

Figure S3 illustrates the effect of combining multiple post-selected images to improve the signal-to-noise ratio. It is seen that, while signal-to-noise ratio improves by increasing n, there is also a decrease in contrast, indicating the existence of a tradeoff in choosing the optimal n. The contrast of different experimental results is shown in Table S1.

	$\Gamma^1_{post}(\%)$	$\Gamma^3_{post}(\%)$	$\Gamma^6_{post}(\%)$	$\Gamma_s(\%)$	$g^{(1)}(\%)$
biphoton imaging (Fig 4)	21.7	15.6	9.5	5.3	3.0
biphoton imaging (Fig. 3)	12.3	8.4	6.2	4.3	2.6
correlation imaging / low scattering (Fig. 5)	10.8	9.0	9.0	4.8	3.4
correlation imaging / high scattering	4.0	3.8	3	1.1	0.9

Table S1. **MTF values for different $\Gamma^{(n)}_{post}$ compared to the coincidences Γ_s and singles $g^{(1)}$**

.

S3. EXPERIMENTAL RESULTS FOR STATIC SCATTERING.

To further validate the approach under different experimental conditions, we considered a configuration with a single static random mask –applied on SLM2–, placed between the object and the detector. Without scattering before the object, strong spatial correlations are preserved on the object plane. In this configuration, in the absence of any scattering, coincidence imaging is known to give a two-fold enhanced contrast. This enhancement is still observed when SLM2 applies a fixed random phase pattern. As in the previous case, a further enhancement is obtained when considering postselected images, as evidenced by the Fourier spatial spectra **S5**-b, and the cross sections **S5**-c.

From the Fourier spectra, we estimated the MTF to be 3.0% for singles ($g^{(1)}$), 5.3% for non-post-selected coincidences (Γ_s), and 15.6% for post-selected coincidences $\Gamma^{(n=3)}_{pos}$. Post-selection provides more than a five-fold improvement over singles and approximately a three-fold improvement compared to the non-post-selected coincidences.

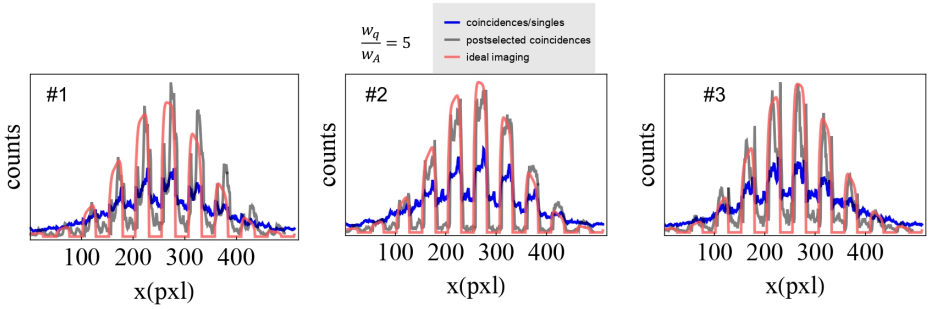


Figure S1. **Simulated results for single realizations of scattering**. Examples of 3 different realizations of the effect of scattering on the MTF. In all cases, postselection leads to contrast improvement, although image distortions, appearing as count fluctuations, are introduced.

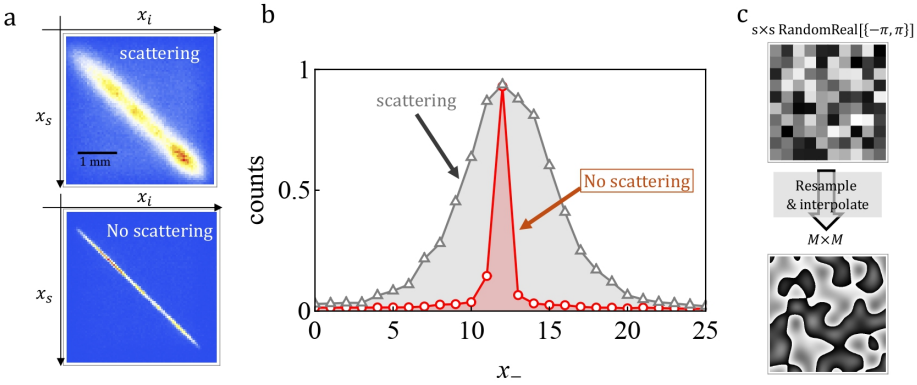


Figure S2. **Scattering characterization and SLM mask generation**. (a) Measured correlations with and without scattering with correlation broadening highlighted in (b). (c) Illustration of the procedure for preparing the phase masks.

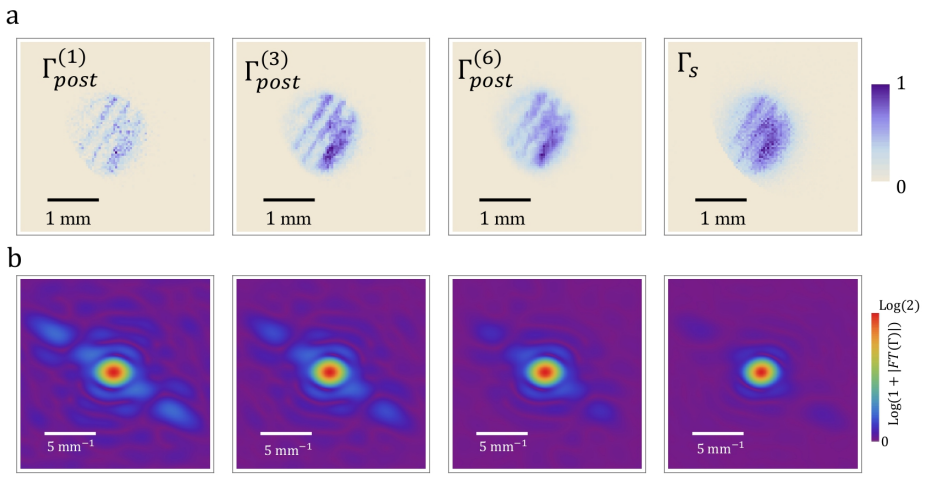


Figure S3. **Results for different numbers of postselection n.**

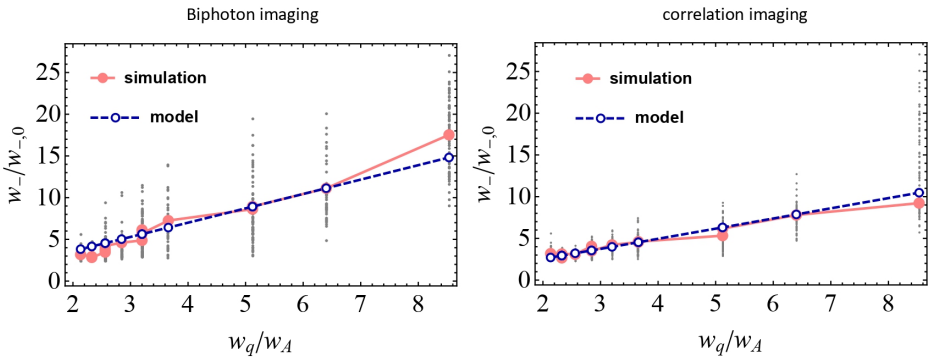


Figure S4. **Simulated correlation broadening as a function of correlation strength** . Simulations were carried out considering 40 realizations (gray dots) of the same scattering strength and averaging over the results. The simulation window had $M = 2^7$ pixels, with $w_q = 0.2M$ and $w_0 = w_q/15$. The results are compared with formulas S1 and S2 for the biphoton and correlation imaging, respectively.

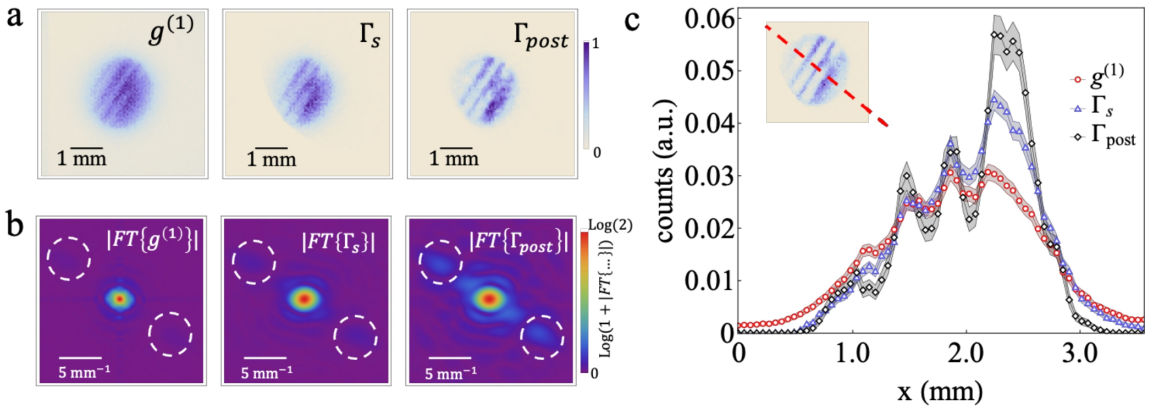


Figure S5. **Contrast enhancement with scattering medium between camera and object. a** Image of the object hidden behind a static scattering medium as reconstructed by singles ($g^{(1)}$), coincidences (Γ_s), and post-selected coincidences ($\Gamma^{(3)}_{post}$). $\Gamma^{(3)}_{post}$ demonstrates an enhanced contrast, as highlighted in **b** and **c**. **b**, 2D Fourier spatial spectra of the images in **a**. The contrast enhancement corresponds to the increased relative brightness of the spatial frequencies evidenced by the dashed white circles. All 2D plots are normalized with respect to the maximum. From the results in **b**, we estimated the MTF to be $3.05\,\%, 5.3\,\%$, and $15.6\,\%$, respectively. **c,** 1D cross-section of each image (indicated by the dashed red line in the inset) with error bands corresponding to 3 times the standard error. In this example, a contrast enhancement is also seen for Γ_s due to the two photons being correlated on the object plane. The scattering strength is, as in Fig. 3, $w_q/w_A \approx 3.4$.

4

Conclusion and Overview

In this thesis, we have introduced a method for enhancing the contrast of objects embedded in weakly scattering media using spatially entangled photon pairs. The basics of the field, from the concepts of image contrast and scattering to the degrees of freedom of light, were covered to motivate and understand the work presented. The theoretical background was then developed, from the quantization of the electromagnetic field and the second-order coherence function to spontaneous parametric down-conversion and the spatial and

temporal correlations of the biphoton state, familiarizing the reader with the key concepts of quantum imaging on which the experiment relies.

The central idea is that the spatial correlations of entangled photon pairs offer a way to distinguish ballistic from scattered light. Ballistic biphotons preserve the strong position correlation imprinted at the source, whereas scattered pairs lose it; by recording spatially resolved coincidences and post-selecting only those events consistent with the original correlation, we isolate the ballistic contribution and, at the same time, reject the uncorrelated background that ordinarily floods the detector. We quantified the resulting improvement through the modulation transfer function and confirmed it both in numerical simulations and in experiments, under static and dynamic scattering conditions.

The method was demonstrated in two configurations: one in which both photons of the pair traverse the scattering medium, and one in which only a single photon does while its partner follows an undisturbed reference path. In both cases, correlation post-selection recovered object features that were washed out in the ordinary single-photon and non-post-selected coincidence images, yielding contrast gains of up to roughly three-fold over non-post-selected coincidences and five-fold over classical single-photon imaging. Because post-selection discards events and therefore increases shot noise, we showed that combining events from several post-selection windows partially restores the signal while preserving the contrast advantage.

A natural next step is to extend the technique to more strongly scattering media. As the scattering strength grows, fewer ballistic pairs survive, and the approach could be

combined with adaptive optics to correct the residual distortions and push the method toward the thicker, more realistic media encountered in biological tissue or turbid water.

Several other directions remain open. The method's performance depends on the degree of spatial entanglement of the source, so brighter, higher-dimensional biphoton sources and faster single-photon-sensitive cameras would improve both the achievable contrast and the acquisition time. One could also ask how the technique transfers to other degrees of freedom — temporal, spectral, or polarization correlations — and whether these can be combined with the spatial post-selection used here. Finally, since the approach operates in regimes where time gating, spatial filtering, and adaptive optics alone are impractical, it is worth exploring where quantum-correlation imaging offers a genuine advantage over classical strategies, and how it might be integrated into practical imaging systems.

References

[1] M. Born and E. Wolf, *Principles of Optics*, 7th (expanded) ed. (Cambridge University Press, Cambridge, 1999).

[2] V. Ntziachristos, "Going deeper than microscopy: the optical imaging frontier in biology," *Nature Methods* **7**, 603–614 (2010).

[3] A. P. Mosk, A. Lagendijk, G. Lerosey, and M. Fink, "Controlling waves in space and time for imaging and focusing in complex media," *Nature Photonics* **6**, 283–292 (2012).

[4] S. Rotter and S. Gigan, "Light fields in complex media: Mesoscopic scattering meets wave control," *Reviews of Modern Physics* **89**, 015005 (2017).

[5] P.-A. Moreau, E. Toninelli, T. Gregory, and M. J. Padgett, "Imaging with quantum states of light," *Nature Reviews Physics* **1**, 367–380 (2019).

[6] T. B. Pittman, Y. H. Shih, D. V. Strekalov, and A. V. Sergienko, "Optical imaging by means of two-photon quantum entanglement," *Physical Review A* **52**, R3429–R3432 (1995).

[7] H. Defienne, M. Reichert, J. W. Fleischer, and D. Faccio, "Quantum image distillation," *Science Advances* **5**, eaax0307 (2019).

[8] T. Gregory, P.-A. Moreau, E. Toninelli, and M. J. Padgett, "Imaging through noise with quantum illumination," *Science Advances* **6**, eaay2652 (2020).

[9] J. C. Maxwell, "A Dynamical Theory of the Electromagnetic Field," *Philosophical Transactions of the Royal Society of London* **155**, 459–512 (1865).

[10] W. Wien, "Über die Energieverteilung im Emissionsspektrum eines schwarzen Körpers," *Annalen der Physik* (1896).

[11] Lord Rayleigh, "Remarks upon the law of complete radiation," *Philosophical Magazine* **49**, 539–540 (1900).

[12] M. Planck, "Über das Gesetz der Energieverteilung im Normalspektrum," *Annalen der Physik* **4**, 553–563 (1901).

[13] A. Einstein, "Über einen die Erzeugung und Verwandlung des Lichtes betreffenden heuristischen Gesichtspunkt," *Annalen der Physik* **17**, 132–148 (1905).

[14] L. Allen, M. W. Beijersbergen, R. J. C. Spreeuw, and J. P. Woerdman, "Orbital Angular Momentum of Light and the Transformation of Laguerre–Gaussian Laser Modes," *Physical Review A* **45**, 8185–8189 (1992).

[15] J. Brendel, N. Gisin, W. Tittel, and H. Zbinden, "Pulsed Energy-Time Entangled Twin-Photon Source for Quantum Communication," *Physical Review Letters* **82**, 2594–2597 (1999).

[16] G. P. Agrawal, *Fiber-Optic Communication Systems*, 4th ed. (Wiley, Hoboken, NJ, 2010).

[17] P. J. Winzer, D. T. Neilson, and A. R. Chraplyvy, "Fiber-optic transmission and networking: the previous 20 and the next 20 years," *Optics Express* **26**, 24190–24239 (2018).

[18] R. J. Glauber, "The Quantum Theory of Optical Coherence," *Physical Review* **130**, 2529–2539 (1963).

[19] R. Hanbury Brown and R. Q. Twiss, "Correlation between Photons in two Coherent Beams of Light," *Nature* **177**, 27–29 (1956).

[20] M. O. Scully and M. S. Zubairy, *Quantum Optics* (Cambridge University Press, Cambridge, 1997).

[21] C. K. Hong, Z. Y. Ou, and L. Mandel, "Measurement of subpicosecond time intervals between two photons by interference," *Physical Review Letters* **59**, 2044–2046 (1987).

[22] S. P. Walborn, C. H. Monken, S. Pádua, and P. H. Souto Ribeiro, "Spatial correlations in parametric down-conversion," *Physics Reports* **495**, 87–139 (2010).

[23] R. Loudon, *The Quantum Theory of Light*, 3rd ed. (Oxford University Press, Oxford, 2000).

[24] C. C. Gerry and P. L. Knight, *Introductory Quantum Optics* (Cambridge University Press, Cambridge, 2005).

[25] R. J. Glauber, "Coherent and Incoherent States of the Radiation Field," *Physical Review* **131**, 2766–2788 (1963).

[26] E. C. G. Sudarshan, "Equivalence of Semiclassical and Quantum Mechanical Descriptions of Statistical Light Beams," *Physical Review Letters* **10**, 277–279 (1963).

[27] J. S. Bell, "On the Einstein Podolsky Rosen Paradox," *Physics* **1**, 195–200 (1964).

[28] R. W. Boyd, *Nonlinear Optics*, 3rd ed. (Academic Press, Burlington, MA, 2008).

[29] D. C. Burnham and D. L. Weinberg, "Observation of Simultaneity in Parametric Production of Optical Photon Pairs," *Physical Review Letters* **25**, 84–87 (1970).

[30] C. K. Hong and L. Mandel, "Theory of parametric frequency down conversion of light," *Physical Review A* **31**, 2409–2418 (1985).

[31] A. D'Errico, F. Hufnagel, F. Miatto, M. Rezaee, and E. Karimi, "Full-mode characterization of correlated photon pairs generated in spontaneous down-conversion," *Optics Letters* **46**, 2388–2391 (2021).

[32] Wikipedia contributors, "Spontaneous parametric down-conversion," *Wikipedia, The Free Encyclopedia*, `https://en.wikipedia.org/wiki/Spontaneous_parametric_down-conversion` (accessed 2026).

[33] P. G. Kwiat, K. Mattle, H. Weinfurter, A. Zeilinger, A. V. Sergienko, and Y. Shih, "New High-Intensity Source of Polarization-Entangled Photon Pairs," *Physical Review Letters* **75**, 4337–4341 (1995).

[34] P. G. Kwiat, E. Waks, A. G. White, I. Appelbaum, and P. H. Eberhard, "Ultrabright source of polarization-entangled photons," *Physical Review A* **60**, R773–R776 (1999).

[35] C. Howard, R. Ghobadi, N. Dehghan, A. D'Errico, and E. Karimi, "Imaging Walk-Off-Driven Distortions in EPR Photon-Pair Correlations," arXiv:2512.12423 (2025).

[36] A. D'Errico and E. Karimi, "Imaging of Biphoton States: Fundamentals and Applications," *Advanced Functional Materials* (2026), doi:10.1002/adfm.202526562.

[37] N. Dehghan, A. D'Errico, F. Di Colandrea, and E. Karimi, "Biphoton state reconstruction via phase retrieval methods," *Optica* **11**, 1115–1123 (2024).

[38] S. Pancharatnam, "Generalized theory of interference, and its applications," *Proceedings of the Indian Academy of Sciences A* **44**, 247–262 (1956).

[39] M. V. Berry, "Quantal phase factors accompanying adiabatic changes," *Proceedings of the Royal Society of London A* **392**, 45–57 (1984).